J. Fluid Mech. (2000), *vol.* 425, *pp.* 301–334. Printed in the United Kingdom

On the three-dimensional interaction of a rotor-tip vortex with a cylindrical surface

By THOMAS D. RADCLIFF[1], ODUS R. BURGGRAF[2] AND A. T. CONLISK[2]

[1]The University of Akron, Akron, Ohio, USA

[2]The Ohio State University, Columbus, Ohio, USA

(Received 7 October 1999 and in revised form 17 June 2000)

The collision of a strong vortex with a surface is an important problem because significant impulsive loads may be generated. Prediction of helicopter fatigue lifetime may be limited by an inability to predict these loads accurately. Experimental results for the impingement of a helicopter rotor-tip vortex on a cylindrical airframe show a suction peak on the top of the airframe that strengthens and then weakens within milliseconds. A simple line-vortex model can predict the experimental results if the vortex is at least two vortex-core radii away from the airframe. After this, the model predicts continually deepening rather than lessening suction as the vortex stretches. Experimental results suggest that axial flow within the core of a tip vortex has an impact on the airframe pressure distribution upon close approach. The mechanism for this is hypothesized to be the inviscid redistribution of the vorticity field within the vortex as the axial velocity stagnates. Two models of a tip vortex with axial flow are considered. First, a classical axisymmetric line vortex with a cutoff parameter is superimposed with vortex ringlets suitably placed to represent the helically wound vortex shed by the rotor tip. Thus, inclusion of axial flow is found to advect vortex core thinning away from the point of closest interaction as the vortex stretches around the cylindrical surface during the collision process. With less local thinning, vorticity in the cutoff parameter model significantly overlaps the solid cylinder in an unphysical manner, highlighting the fact that the vortex core must deform from its original cylindrical shape. A second model is then developed in which axial and azimuthal vorticity are confined within a rectangular-section vortex. Area and aspect ratio of this vortex can be varied independently to simulate deformation of the vortex core. Both axial velocity and core deformation are shown to be important to calculate the local induced pressure loads properly. The computational results are compared with experiments conducted at the Georgia Institute of Technology.

1. Introduction

The flow field about a helicopter in flight is complex in structure. There is a downwash velocity field, strong tip vortex and inboard vortex sheet generated by the rotor superimposed on the mean flow around the airframe of the rotorcraft. In particular, the strong tip vortex can cause significant pressure loading and noise as it interacts with the airframe. This problem is exacerbated as design requirements place the rotor and airframe in closer proximity. Precise details of the collision of the tip vortex with the airframe, as depicted on figure 1, have not been resolved because of a lack of understanding of the local physics of the problem. Also, the wide range

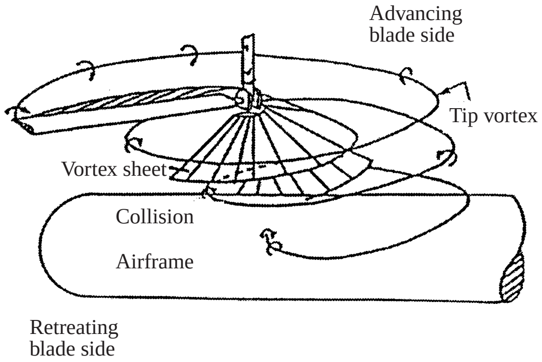

FIGURE 1. The wake of a single-bladed rotor in low-speed forward flight.

of spatial and temporal scales involved can make detailed CFD modelling of the collision intractable. Thus, in the large-scale rotor codes used to predict rotorcraft behaviour, heuristic methods have been used to describe the vortex path when the vortex comes to within one core radius of the airframe. As an example, rotor codes often prevent the vortex centreline from coming within a fixed distance of the airframe (Lorber & Egolf 1990). Such arbitrary methods of describing the intense interaction between a vortex and a surface limit our ability to accurately predict the airframe pressure distribution and hence the vortex loading. In this paper we consider the direct collision of a rotor-tip vortex with a cylindrical airframe.

At this point, we should define what we refer to as a vortex-boundary 'collision'. Consider the case where the scale of the vortex is much smaller than the body scale. A 'collision' is then defined as the physical process in which a portion of the vortex, a region of concentrated vorticity surrounded by irrotational fluid, merges with and ultimately cannot be distinguished from the boundary-layer fluid. For a strong vortex, this transition is initially dominated by inviscid phenomena such as vorticity redistribution caused by interaction of the axial-flow vortex with the solid surface (Lee, Burggraf & Conlisk 1998) and vortex cross-sectional distortion.

Considerable numerical and experimental work devoted to prediction of the rotor-tip vortex trajectory in the vicinity of an airframe and induced pressure on the airframe has been presented in the literature. Tip-vortex trajectories in the vicinity of an airframe (Scully 1975; Egolf & Landgrebe 1983) have been shown to be well-modelled by potential flow methods using a vortex velocity field described by the modified Biot-Savart law. The modification adds a cutoff parameter μ (Batchelor 1967; Widnall, Bliss & Zalay 1971; Moore & Saffman 1972) that has the effect of distributing the vorticity and thus preventing infinite propagation speed of a curved vortex (Hon & Walker 1991). Recent results that apply a segmented, fixed-core-radius rotor-tip-vortex model to evaluate the vortex trajectory in the potential flow surrounding a cylindrical airframe (Affes & Conlisk 1993; Affes *et al.* 1993; Xiao, Affes & Conlisk 1994) indicate that when the vortex is more than two core radii away from the airframe, the μ-distributed model for the vortex core allows prediction of experimental vortex trajectories (Liou, Komerath & McMahon 1990) and the pressure measured on top of the airframe (Brand 1989) with reasonable accuracy.

During this early time frame, a suction peak forms on the airframe beneath the vortex. As the vortex approaches the airframe, this peak gradually strengthens with a magnitude that depends principally on the vortex circulation. This magnitude is not yet substantially influenced by the local properties of the vortex, such as local

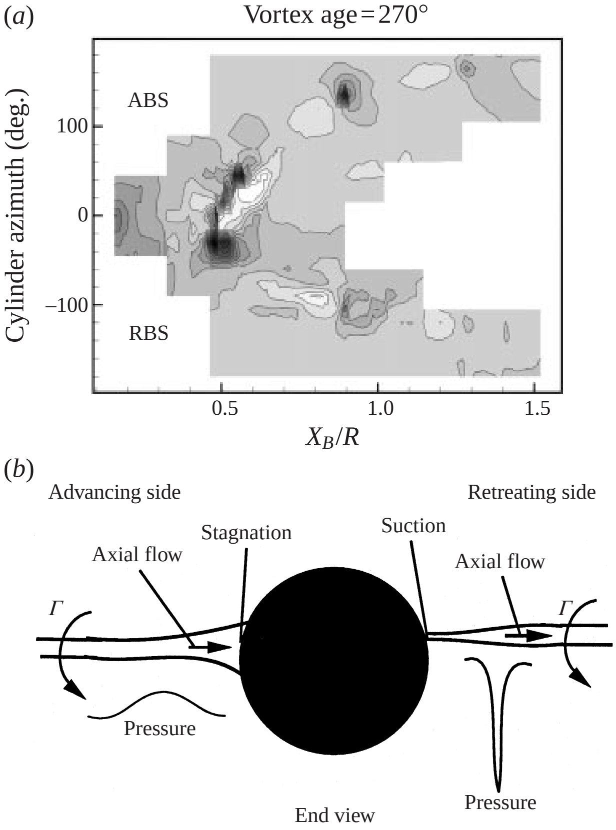

FIGURE 2. (*a*) Pressure distribution around a model airframe at $\psi = 270°$ as measured by Kim & Komerath (1995), showing the differences exhibited on the advancing and retreating sides of the airframe. The pressure coefficient ranges from −4.3 in the black areas to 1.2 in the white. The angle ϕ measures the azimuth from the top of the cylinder, and $\phi > 0$ denotes the advancing blade side. X_B/R measures the distance along the airframe in the forward flight direction. (*b*) A sketch of the tip-vortex structure along the sides of the airframe as described by Kim & Komerath (1995) and Lee *et al.* (1998). The vortex core radius is greatly enlarged for clarity.

vortex stretching, core cross-sectional shape or axial velocity in the core. As the vortex moves closer and finally collides with the airframe, experimental observations indicate asymmetries along the vortex axis in vortex trajectory, core radius and surface pressure as well as an eventual weakening of the suction peak at the top of the airframe (Kim & Komerath 1995; Mahalingam *et al.* 1995) that cannot be predicted by an axisymmetric μ-distributed vortex model.

Careful study of the experimental vortex–airframe interaction, visualized by synchronized copper-vapour laser-pulse illumination of smoke-seeded vortices, suggests that two effects not previously modelled could cause the observed behaviour: axial velocity in the vortex core and flattening of the vortex core on close approach. We first consider the effects of axial velocity. The tip vortex shed from a helicopter rotor blade is typical of all tip vortices shed from loaded wings in forward motion in that there is present within the core a significant velocity oriented along the generators of the vortex (McAlister *et al.* 1995). Experimental results for pressure on the airframe surface at a rotor phase angle of $\psi = 270°$ and an advance ratio 0.1 are shown on figure 2 (Kim & Komerath 1995). The rotor phase angle ψ is defined as the angle between the rotor blade and the generators of the airframe. For this advance ratio, the

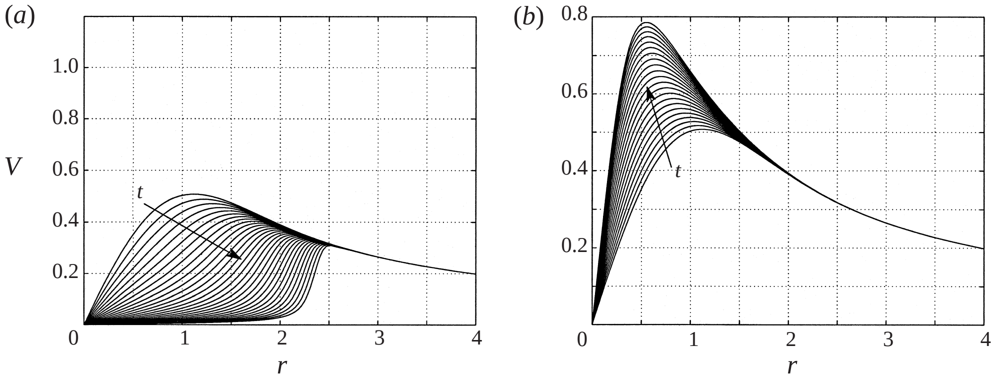

FIGURE 3. Swirl velocity V as a function of radius r on a surface, impulsively inserted through an axial-flow vortex, at various times after insertion. Here, the dimensionless circulation is $\Gamma = 5$. (*a*) Advancing blade side with axial flow toward the wall. (*b*) Retreating blade side with axial flow away from the wall.

actual collision process begins at approximately $\psi = 228°$. Note that on the retreating blade side (RBS), the newest suction peak near $X_B/R = 0.5$ is still strongly focused, while on the advancing blade side (ABS), the pressure on the airframe at a point coinciding with the vortex core is more diffuse. The observed vortex configuration corresponding to this pressure distribution is sketched in figure 2(*b*).

Axial flow in the vortex core can cause the observed effects through inviscid vorticity advection near the airframe surface during a collision. This phenomenon has been demonstrated by a model in which a surface is impulsively inserted through an initially infinite vortex with a fully-developed axial velocity profile to create two semi-infinite vortices (Lee *et al.* 1998). In that study, the axisymmetric unsteady Euler equations were solved to determine the velocity field within these semi-infinite vortices on the inserted surface after the vortex is severed. When the axial velocity in the core of the vortex is directed toward the surface, depicted in figure 3(*a*), vorticity is advected outward and the swirl on the wall decreases as time advances. Note that the location of maximum swirl velocity that defines the vortex core radius has moved outward, indicating a bulge in the vortex; moreover, the solution appears to be approaching a steady state. Similar results have been produced for the case where the axial velocity is away from the wall, as depicted in figure 3(*b*). Here, we note the inward advection and focusing of the swirl that leads to a steepening suction peak. These features are similar to what is depicted in the experimental results of figure 2.

Recently, the model of Xiao *et al.* (1994), which describes the interaction of a modified line vortex with an airframe represented by a distribution of source-panels, has been modified to incorporate the effects of axial flow through the addition of vortex rings centred about the axis of the line vortex. Evaluation of the vortex trajectory and core radius for fundamental mean flow conditions (Radcliff, Burggraf & Conlisk 1997) demonstrate that the bulging and thinning seen in experiments are predicted. An attempt to predict the pressure measured during experiments using this axial-flow model (Mahalingam *et al.* 1997) captures much of the asymmetry that could not be predicted previously, but the reduction in pressure loading observed as the collision process proceeds was not predicted. This phenomenon, which begins when the vortex axis is within one core radius of the top of the airframe, is strongly correlated with observed deformation (flattening) of the vortex core.

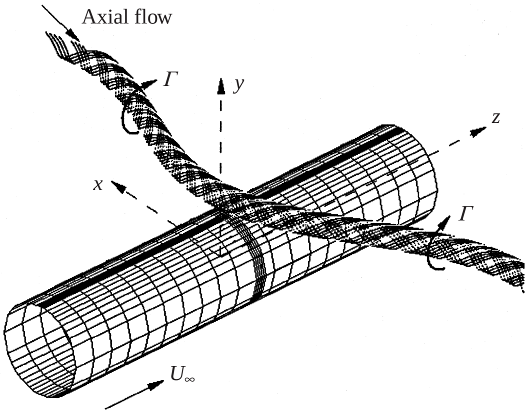

FIGURE 4. Panel airframe and helical vortex system representations with the global coordinate system used in the calculations.

In this paper, we present a vortex model which incorporates azimuthal and axial velocity from a superposition of modified line and ring vortex components initially developed by Radcliff *et al.* (1997). This model is then modified to allow vortex-core deformation through distribution of axial and azimuthal vorticity within a vortex core of rectangular cross-section whose aspect ratio can be varied (Radcliff *et al.* 1999). These two vortex models, combined with representations of the airframe and mean flow, are used to evaluate airframe surface-pressure loading. The results are then compared with experiments.

2. Interaction modelling with an axisymmetric axial-flow vortex

To predict the airframe surface pressures measured in experiments, a model of the global vortex–airframe velocity field and vortex movement in close proximity to the surface is required. The model we have produced employs five components; an analytical representation of the vortex velocity field, a source-panel model to enforce the zero-normal-velocity boundary condition at the airframe surface, a representation of the mean flow surrounding the airframe including the rotor downwash, a Lagrangian scheme to propagate the vortex in space and a calculation of the surface pressure from the surface velocity field. Figure 4 depicts the modelled vortex–airframe system. Note that the z-axis in these global coordinates corresponds to the X_B-axis in the experimental references and in figure 2. The individual model components are discussed below.

2.1. *Vortex velocity field – axial vorticity*

A rotor-tip vortex develops when vorticity shed by a rotor wraps up locally, resulting in a trailing region of highly concentrated vorticity as the rotor moves forward (McAlister *et al.* 1995). The resulting vortex may be approximately represented by a continuous distribution of helical vortices along a cylinder whose radius represents the vortex core. Note that in this representation the helical vortices have axial and azimuthal vorticity components relative to the overall tip-vortex axis and will induce swirl and axial velocity fields, respectively. A similar velocity distribution may be produced by the superposition of axially oriented line vortices distributed about the tip-vortex core radius and azimuthally oriented ring vortices, with a radius equal to the tip-vortex core radius, distributed along the vortex axis. The line vortices will induce the aforementioned azimuthal velocity component, while the rings will induce radial and

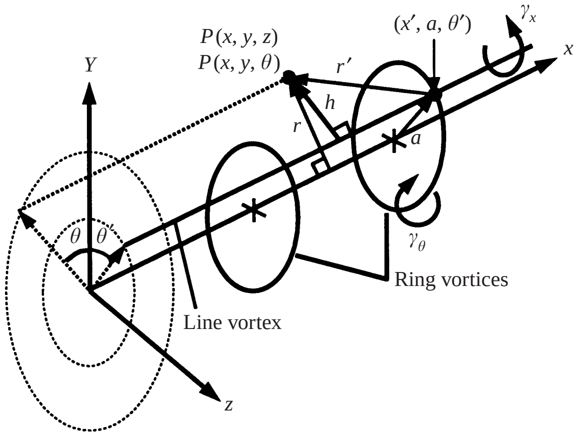

FIGURE 5. Configuration of the axisymmetric vortex and parameters for calculation of the vortex velocity components.

axial velocity. The advance angle of the helical vortex can then be represented by the apportionment of axial and azimuthal circulation given a fixed total vortex circulation. In this section, the velocity distributions caused by a semi-infinite tip vortex with line and ring components will be derived. A finite segment of such a vortex may then be created by superposition of two semi-infinite vortices of opposite sign.

A local cylindrical coordinate system is first defined in which x is the distance measured along the axis of the vortex cylinder, r is the radial distance from the vortex centreline, and θ is the azimuthal angle. The origin is located in the end plane of the semi-infinite cylinder, as shown in figure 5. We let a represent the radius of the cylindrical vortex sheet and Γ the total circulation of the flow around the vortex cylinder. Let γ_x be the circulation of the axial vortices per unit width of an axial strip along the cylinder surface and γ_θ the circulation of the ring vortices per unit length along the cylinder surface. Then $\gamma_x = \Gamma/2\pi a$, and γ_θ depends on the advance angle β of the original helical vortices.

We first consider the axial vorticity represented by the distribution of line vortices. For temporary convenience, we define a Cartesian coordinate system with y and z axes in the end plane of the vortex cylinder and place an elementary line vortex strip parallel to the x-axis on the core radius a, also shown in figure 5. The circulation of such a strip is $\mathrm{d}\Gamma_x = \gamma_x a\,\mathrm{d}\theta'$, where $\mathrm{d}\theta'$ is the angular width of the strip. The velocity induced by the vortex strip at a point $P(x, y, z)$ is perpendicular to the meridian plane formed by the vortex line itself and any ray from the vortex to the point P. Consider the Biot-Savart law (Batchelor 1967)

$$\mathrm{d}\boldsymbol{v} = \frac{1}{4\pi}\frac{\mathrm{d}\boldsymbol{\Gamma} \times \boldsymbol{r}'}{r'^3}, \tag{2.1}$$

where $\boldsymbol{v}$ is the induced velocity, $\mathrm{d}\boldsymbol{\Gamma}$ is the circulation of the differential vortex strip and $\boldsymbol{r}'$ is a vector from the vortex element to the object point with length r'. The magnitude of the induced velocity at P is found by integrating from $x' = 0$ to ∞, giving a well-known formula

$$v_{\theta'} = \frac{\Gamma_x}{4\pi h}\left(1 + \frac{x}{\sqrt{x^2 + h^2}}\right), \tag{2.2}$$

where h is the perpendicular distance from the vortex strip to the point P. Denoting the angle measured around the cylinder from the y-axis to the vortex strip by θ', as depicted in figure 5, we find

$$h = \sqrt{(y - a\cos\theta')^2 + (z - a\sin\theta')^2}$$
$$= \sqrt{r^2 + a^2 - 2ar\cos(\theta' - \theta)}, \tag{2.3}$$

where r denotes the perpendicular radius from the x-axis to the point P and θ is the angle from the y-axis to P.

The velocity induced by the elementary vortex strip may now be resolved into Cartesian components, as

$$v'_y = -v'_\theta(z - a\sin\theta')/h, \tag{2.4}$$

$$v'_z = v'_\theta(y - a\cos\theta')/h. \tag{2.5}$$

Summing the induced velocity of each such strip around the vortex cylinder yields integral formulae for the total induced velocity

$$v_y = -\frac{\gamma_x a}{4\pi}\int_0^{2\pi}\left(1 + \frac{x}{\sqrt{x^2 + h^2}}\right)\frac{z - a\sin\theta'}{h^2}\,\mathrm{d}\theta', \tag{2.6}$$

$$v_z = \frac{\gamma_x a}{4\pi}\int_0^{2\pi}\left(1 + \frac{x}{\sqrt{x^2 + h^2}}\right)\frac{y - a\cos\theta'}{h^2}\,\mathrm{d}\theta'. \tag{2.7}$$

The radial and azimuthal components in the cylindrical system of the tip vortex are then given by

$$v_r = v_y\cos\theta + v_z\sin\theta, \tag{2.8}$$

$$v_\theta = -v_y\sin\theta + v_z\cos\theta. \tag{2.9}$$

The integrand of v_r is an odd function of θ' and so the integral vanishes, leaving no net radial velocity. The last factor of the integrands in v_y and v_z, when combined into v_θ, may be simplified as follows:

$$\frac{1}{h^2}[(z - a\sin\theta')\sin\theta + (y - a\cos\theta')\cos\theta]$$
$$= \frac{1}{h^2}[z\sin\theta + y\cos\theta - a(\sin\theta\sin\theta' + \cos\theta\cos\theta')]$$
$$= \frac{r - a\cos(\theta' - \theta)}{r^2 + a^2 - 2ar\cos(\theta' - \theta)}. \tag{2.10}$$

Hence, the integral for the azimuthal velocity component becomes

$$v_\theta = \frac{\gamma_x a}{4\pi}\int_0^{2\pi}\left[1 + \frac{x}{\sqrt{x^2 + r^2 + a^2 - 2ar\cos(\theta' - \theta)}}\right]\left[\frac{r - a\cos(\theta' - \theta)}{r^2 + a^2 - 2ar\cos(\theta' - \theta)}\right]\mathrm{d}\theta'. \tag{2.11}$$

Non-dimensionalizing by introducing $\eta = r/a$ and $\xi = x/a$, we define the integrals

$$I_1(\eta) = \int_0^\pi \frac{\eta - \cos\phi}{1 + \eta^2 - 2\eta\cos\phi}\,\mathrm{d}\phi \tag{2.12}$$

and

$$I_2(\xi, \eta) = \int_0^\pi \frac{\eta - \cos\phi}{(1 + \eta^2 - 2\eta\cos\phi)}\left[\frac{1}{\sqrt{1 + \xi^2 + \eta^2 - 2\eta\cos\phi}}\right]\mathrm{d}\phi, \tag{2.13}$$

so the azimuthal velocity can be expressed as

$$v_\theta = \frac{\gamma_x}{2\pi}[I_1(\eta) + \xi I_2(\xi, \eta)]. \tag{2.14}$$

The integrals I_1 and I_2 can be represented as complete elliptic integrals. Recalling that $\gamma_x = \Gamma/2\pi a$, we obtain the final result

$$v_\theta = \frac{\Gamma}{4\pi r}\left\{\tfrac{1}{2}[1 + \operatorname{sgn}(r-a)] + \frac{1}{\pi}\frac{x}{\sqrt{x^2+(r+a)^2}}\left[K(k) + \frac{r-a}{r+a}\Pi(\sigma^2, k)\right]\right\}, \tag{2.15}$$

where $K(k)$ is the complete elliptic integral of the first kind and $\Pi(\sigma^2, k)$ is the complete elliptic integral of the third kind. (We use the definition of Byrd & Friedman for the elliptic integrals where σ^2 corresponds to the modulus n of Abramowitz & Stegun (1964).) The moduli are defined as

$$k^2 = \frac{4ar}{x^2 + (r+a)^2} \tag{2.16}$$

and

$$\sigma^2 = \frac{4ar}{(r+a)^2}. \tag{2.17}$$

2.2. *Vortex velocity field–azimuthal vorticity*

The azimuthal vorticity component is represented by vortex rings distributed uniformly along the vortex cylinder. We proceed in the same manner as before, the only difference being the direction of the vortex elements. Consider a differential element of the surface vorticity in the form of a rectangle with length $\mathrm{d}x'$ and width $\mathrm{d}s = a\,\mathrm{d}\theta'$, located about (x', a, θ') in the cylindrical coordinate system of the tip vortex. The velocity vector at an object point $P(x, r, \theta)$ for an element with circulation $\mathrm{d}\boldsymbol{\Gamma} = \gamma_\theta\,\mathrm{d}x'\,\mathrm{d}\boldsymbol{s}$ has the vector form

$$\mathrm{d}\boldsymbol{v}' = \frac{\gamma_\theta}{4\pi r'^3}\,\mathrm{d}x'\,\mathrm{d}\boldsymbol{s} \times \boldsymbol{r}', \tag{2.18}$$

where r' is evaluated as

$$r' = [(x-x')^2 + r^2 + a^2 - 2ar\cos(\theta - \theta')]^{1/2}. \tag{2.19}$$

The non-zero components of $\mathrm{d}\boldsymbol{v}'$ are found to be

$$\mathrm{d}v_r' = \frac{\gamma_\theta\,\mathrm{d}s}{4\pi r'^3}(x - x')[\cos(\theta - \theta')]\,\mathrm{d}x', \tag{2.20}$$

$$\mathrm{d}v_x' = \frac{\gamma_\theta\,\mathrm{d}s}{4\pi r'^3}[a - r\cos(\theta - \theta')]\,\mathrm{d}x'. \tag{2.21}$$

The induced velocity of a semi-infinite strip of such lateral vortices is generated by integrating with respect to the surface vortex element coordinate x' from 0 to ∞:

$$\mathrm{d}v_r = \frac{\gamma_\theta\,\mathrm{d}s}{4\pi}\int_0^\infty \frac{(x-x')[\cos(\theta - \theta')]}{r'^3}\,\mathrm{d}x', \tag{2.22}$$

$$\mathrm{d}v_x = \frac{\gamma_\theta\,\mathrm{d}s}{4\pi}\int_0^\infty \frac{a - r\cos(\theta - \theta')}{r'^3}\,\mathrm{d}x'. \tag{2.23}$$

Note that $\mathrm{d}v_r$ is parallel to the ray from the axis of the vortex cylinder through the strip. The result of the integration is

$$\mathrm{d}v_r = -\frac{\gamma_\theta\,\mathrm{d}s}{4\pi}\frac{\cos(\theta-\theta')}{\sqrt{x^2+r^2+a^2-2ar\cos(\theta-\theta')}}, \tag{2.24}$$

$$\mathrm{d}v_x = \frac{\gamma_\theta\,\mathrm{d}s}{4\pi}\frac{a-r\cos(\theta-\theta')}{r^2+a^2-2ar\cos(\theta-\theta')}\left[1+\frac{x}{\sqrt{x^2+r^2+a^2-2ar\cos(\theta-\theta')}}\right]. \tag{2.25}$$

Now we set $\mathrm{d}s = a\,\mathrm{d}\theta'$ and integrate around the cylinder. Note that the azimuthal velocity component cancels out, since pairs of vortex strips at $\theta' = \theta + \Delta\theta$ and $\theta' = \theta - \Delta\theta$ produce the same radial velocity in the direction of their own radii. Hence, the non-vanishing velocity components for the complete semi-infinite vortex cylinder are

$$v_r = \frac{\gamma_\theta\,a}{4\pi}\int_{\theta-\pi}^{\theta+\pi}\frac{\cos(\theta-\theta')}{\sqrt{x^2+r^2+a^2-2ar\cos(\theta-\theta')}}\,\mathrm{d}\theta', \tag{2.26}$$

and

$$v_x = \frac{\gamma_\theta\,a}{4\pi}\int_{\theta-\pi}^{\theta+\pi}\frac{a-r\cos(\theta-\theta')}{r^2+a^2-2ar\cos(\theta-\theta')}\left[1+\frac{x}{\sqrt{x^2+r^2+a^2-2ar\cos(\theta-\theta')}}\right]\mathrm{d}\theta'. \tag{2.27}$$

Non-dimensionalizing as before, these velocities can also be expressed in terms of elliptic integrals. To evaluate v_r, we define the integral

$$I_0(\xi,\eta) = \int_0^\pi \frac{\cos\phi}{\sqrt{1+\xi^2+\eta^2-2\eta\cos\phi}}\,\mathrm{d}\phi, \tag{2.28}$$

and with I_1 and I_2 defined as before these velocities become

$$v_r = -\frac{\gamma_\theta}{2\pi}\,\eta\,I_0(\xi,\eta), \tag{2.29}$$

and

$$v_x = \frac{\gamma_\theta}{2\pi}\,\eta[I_1(\eta)+\xi\,I_2(\xi,\eta)]. \tag{2.30}$$

Evaluating the radial velocity component gives

$$v_r = -\frac{\gamma_\theta\,a}{2\pi r}\sqrt{x^2+(a+r)^2}\left[\frac{x^2+a^2+r^2}{x^2+(a+r)^2}K(k)-E(k)\right], \tag{2.31}$$

where $E(k)$ is the complete elliptic integral of the second kind, while the axial component becomes

$$v_x = \frac{\gamma_\theta}{4}\left\{[1+\operatorname{sgn}(a-r)]+\frac{2}{\pi}\frac{x}{\sqrt{x^2+(a+r)^2}}\left[K(k)-\frac{r-a}{r+a}\Pi(\sigma^2,k)\right]\right\}. \tag{2.32}$$

Finally, the value of γ_θ for the vortex rings can be deduced from the helical-vortex distribution as follows. Consider a small triangular element of the surface of the vortex cylinder, for which the hypotenuse lies along the helically wrapped vortex line and the base is parallel to the cylinder axis, as shown on figure 6. Denote by β the angle between the base and the hypotenuse; i.e. the advance ratio of the helix is $\tan\beta$. All of the vortex lines that pass through the base also pass through the height, and vice versa. Let the length of the base of the triangle be denoted by b and that of the

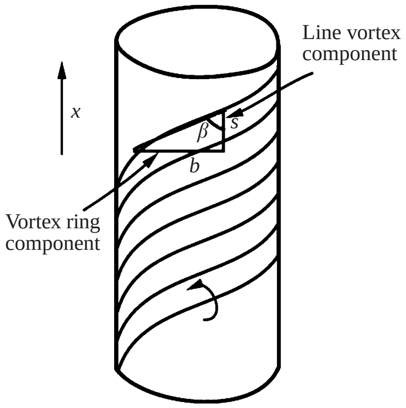

FIGURE 6. Relationship between the azimuthal and axial components of circulation on the axial-flow vortex.

height by s. Then, if there are n vortex lines crossing the base, each of circulation Γ_1, the vortex density along the base is $n\Gamma_1/b$, and its perpendicular (azimuthal) component is $\gamma_\theta = (n\Gamma_1/b)\sin\beta$. Similarly, for the height, the axial component is $\gamma_x = (n\Gamma_1/s)\cos\beta$. The ratio is thus

$$\frac{\gamma_\theta}{\gamma_x} = \frac{s}{b}\tan\beta = \tan^2\beta. \tag{2.33}$$

However, we have already noted that $\gamma_x = \Gamma/2\pi a$, where Γ is the total circulation of the vortex cylinder, so

$$\gamma_\theta = \frac{\Gamma}{2\pi a}\tan^2\beta. \tag{2.34}$$

Although the formulation just described is perhaps the simplest representation of a fully three-dimensional rotor-tip vortex velocity field, concentrating all axial and azimuthal vorticity into a vortex sheet at $r = a$ can result in numerical instability when vortex segments are strung together and allowed to propagate freely. A helico-cylindrical vortex sheet of finite thickness also better approximates the physical situation. This refinement can be accomplished by smoothing the vorticity over the core radius using the cutoff parameter μ.

A μ-vortex is defined by the modified Biot-Savart law, in which r' from the standard Biot-Savart law, equation (2.1), is replaced by $\bar{r}' = \sqrt{r'^2 + \mu^2}$. The finite propagation speed of a vortex ring with a Rankine core of radius a_c is matched (Moore & Saffman 1972) by setting

$$\mu = a_c e^{-3/4}. \tag{2.35}$$

In the present case, we have modelled a finite tip-vortex core by defining line and ring vortices distributed along a specified core radius. Applying a cutoff parameter to both components of this vortex formulation will approximate a continuous distribution of line and ring vortex filaments, thus smoothing the concentrated sheet of vorticity identified previously. Because we want both axial and azimuthal vorticity distributed to the vortex centre, it is appropriate to assume $a_c = a$ for both the line and ring vortex components. Of course, vorticity will also be distributed outward from the core radius when this formulation is applied.

The resulting velocity field may be derived following the same steps as before, but now beginning with the modified Biot-Savart law. The velocity integrals are evaluated as before to give

$$v_\theta = \frac{\Gamma}{4\pi r}\left\{\frac{1}{2}\left[1+\frac{r^2-a^2-\mu^2}{\sqrt{(r^2+a^2+\mu^2)^2-4a^2r^2}}\right]\right.$$
$$\left.+\frac{1}{\pi}\frac{x}{\sqrt{x^2+\mu^2+(r+a)^2}}\left[K(\bar{k})+\frac{r^2-a^2-\mu^2}{(r+a)^2+\mu^2}\Pi(\bar{\sigma}^2,\bar{k})\right]\right\}, \quad (2.36)$$

$$v_r = -\frac{\gamma_\theta}{2\pi r}\sqrt{x^2+\mu^2+(a+r)^2}\left[\frac{x^2+r^2+a^2+\mu^2}{x^2+\mu^2+(a+r)^2}K(\bar{k})-E(\bar{k})\right], \quad (2.37)$$

and

$$v_x = \frac{\gamma_\theta}{4}\left\{\left[1+\frac{a^2-r^2-\mu^2}{\sqrt{(r^2+a^2+\mu^2)^2-4a^2r^2}}\right]\right.$$
$$\left.+\frac{2}{\pi}\frac{x}{\sqrt{x^2+\mu^2+(r+a)^2}}\left[K(\bar{k})+\frac{a^2-r^2-\mu^2}{(a+r)^2+\mu^2}\Pi(\bar{\sigma}^2,\bar{k})\right]\right\}, \quad (2.38)$$

while the moduli defined for the μ-vortices are

$$\bar{k}^2 = \frac{4ar}{x^2+(r+a)^2+\mu^2}, \quad (2.39)$$

$$\bar{\sigma}^2 = \frac{4ar}{(r+a)^2+\mu^2}, \quad (2.40)$$

and the relationship between the circulation Γ of the vortex cylinder and the vorticity components γ_x and γ_θ remains unchanged.

Note that in the classical case of $\mu \rightarrow 0$, a symmetry argument predicts that the axial and azimuthal velocity components as $x \rightarrow \infty$ are exactly double their values for $x = 0$. This result is confirmed by (2.31) and (2.32), where we make use of the limiting results $k \rightarrow 0$ as $x \rightarrow \infty$, and $\Pi(\sigma^2, 0) = \pi/2\sqrt{1-\sigma^2}$. At both x-locations, v_x vanishes for $r > a$ and v_θ vanishes for $r < a$. Also, v_r vanishes identically for $x \rightarrow \infty$, though not for $x = 0$. These conclusions for v_x and v_θ do not hold for the μ-vortex, since the symmetry argument fails in that case, owing to the overlap of vorticity at the opposing ends of the two halves of the infinite vortex-cylinder.

2.3. *Distributed vorticity with zero physical radius – vortex ringlets*

The application of the μ-vortex model to our helical tip-vortex system introduces the possibility of a simplification. Initially, our model consisted of line and ring vortices, unmodified by the cutoff parameter, distributed over the surface of a semi-infinite cylinder of radius a. Collapsing this structure to a physical radius $a = 0$ would give an axial vorticity component identical to a single line vortex, with infinite azimuthal velocity on the vortex axis. The azimuthal vorticity component would collapse to give infinite axial velocity on the vortex system axis given that the ratio of axial to azimuthal circulation β is maintained. Introduction of the cutoff parameter to both line and ring vortex models allows the collapse of the helical vortex system into a meaningful three-dimensional velocity profile; a finite azimuthal velocity profile that peaks at an effective vortex core radius and a finite axial velocity profile that peaks at the vortex centreline. This model, then, provides the detail we want without evaluating the elliptic integrals, an iterative computation that is difficult to vectorize because of data dependency.

The azimuthal velocity component for the zero-physical-radius model is given by a single modified line vortex at the tip-vortex centreline with the aggregate circulation of the original cylindrical line vortex distribution. This velocity field, obtained from (2.36) in the limit $a \to 0$ while holding μ fixed, is

$$v_\theta = \frac{\Gamma_x\, r}{4\pi(r^2+\mu^2)}\left(1+\frac{x}{\sqrt{x^2+r^2+\mu^2}}\right), \tag{2.41}$$

where Γ_x is the total axial circulation of the helical vortices.

Several approaches are possible to derive the zero-radius limit case for the axial and radial velocity components. We can:

(i) Expand the μ-vortex ring elliptic integral formulas (equations (2.37) and (2.38)) in power series;

(ii) Form the expression for a singular vortex ring by expanding the well-known formula for a finite vortex ring (modified with a cutoff parameter) and then integrating it along the axis of the tip-vortex cylinder; or

(iii) Expand the integrands of the μ-modified integrals I_0, I_1 and I_2 in powers of η and discard the higher-order terms prior to evaluating the elliptic integrals.

The third approach is the simplest and is followed here, although each of the three methods listed above were carried out, with identical results for each method. The resulting velocity components are

$$v_r = -\frac{\gamma_\theta\, a^2}{4}\frac{r}{(x^2+r^2+\mu^2)^{3/2}}, \tag{2.42}$$

and

$$v_x = \frac{\gamma_\theta\, a^2}{4}\left\{\frac{2\mu^2}{(r^2+\mu^2)^2} + x\frac{(2\mu^2-r^2)(r^2+\mu^2)+2\mu^2x^2}{(r^2+\mu^2)^2(x^2+r^2+\mu^2)^{3/2}}\right\}. \tag{2.43}$$

We term this the ‘ringlet’ velocity distribution.

Note that these limit forms of the velocity field are useful provided the factors $\Gamma_x = \gamma_x 2\pi a$ and $\gamma_\theta a^2$ are held fixed, equal to their values for the original finite helical vortices. This interpretation is automatic for the axial vortices, but the ringlets may be interpreted more easily in terms of the axial volume flux induced by these vortices. It is convenient to consider the volume flux Q for a fully infinite vortex cylinder, which we obtain by evaluating the limit as $x \to \infty$ to find

$$v_x \longrightarrow \gamma_\theta\, a^2 \frac{\mu^2}{(r^2+\mu^2)^2}. \tag{2.44}$$

Then

$$Q = \int_0^\infty v_x\, 2\pi r\, \mathrm{d}r = \pi\gamma_\theta\, a^2. \tag{2.45}$$

Hence, the former expressions for v_r and v_x may be rewritten in terms of Q, and the physical radius a is suppressed altogether as:

$$v_r = -\frac{Q}{4\pi\mu^2}\frac{r/\mu}{(1+(x^2/\mu^2)+(r^2/\mu^2))^{3/2}}, \tag{2.46}$$

$$v_x = \frac{Q}{4\pi\mu^2}\frac{1}{(1+(r^2/\mu^2))^2}\left\{2+\frac{x}{\mu}\frac{(2-(r^2/\mu^2))(1+(r^2/\mu^2))+2x^2/\mu^2}{(1+(x^2/\mu^2)+(r^2/\mu^2))^{3/2}}\right\}. \tag{2.47}$$

The parameter μ is now seen to be the effective radius of the ringlet vortices, in the sense that the axial velocity scale is obtained by dividing the volume flux Q by an effective cross-sectional area expressed by $\pi\mu^2$.

2.4. *Airframe model*

The airframe represents a zero-normal-velocity boundary condition. We model this with a source-panel method originally due to Hess & Smith (1967) and applied to the present problem by Xiao *et al.* (1994). The airframe is represented by a finite-length circular cylinder which is approximated by $M \times N$ rectangular source panels, where M is the number of panels along the cylinder axis and N is the number of panels around the cylinder. The panel size is not uniform and is designed to be smallest in the region immediately under the vortex. The length of the panels in the axial direction vary according to

$$\Delta L_{Vm} = L_{Vmin} + Bm^2 \quad (m = 1, 2, \ldots, M/2), \tag{2.48}$$

where

$$B = 6\left[\frac{L_{Vmin} - \frac{1}{2}M\Delta L_{Vmin}}{\frac{1}{2}M(\frac{1}{2}M^2+1)}\right], \tag{2.49}$$

L_{Vm} is the length of the mth panel, L_{Vmin} is the minimum panel width and L_{Vmax} is the half length of the airframe cylinder. The panel distribution in the azimuthal direction is also not uniform but is heuristically clustered under the vortex.

The panel mesh is translated axially to maintain the narrowest axial panels directly beneath the head of the approaching vortex, a strategy required by the close approach of the strong vortex to the airframe. Since the panels remain in the same configuration, the matrix of influence coefficients, which is inverted to find the panel source strengths, is independent of time and need not be recalculated at each timestep. The panel representation of the airframe is illustrated in figure 4.

2.5. *Mean flow model*

The flow in the rotor downwash region occupied by the tip-vortex is very complex. Analysis of the vortex trajectory experimentally determined by Liou *et al.* (1990) suggests that the mean flow components in the rotor downwash near the airframe could be reasonably represented by a constant mean flow with a linear shear, such that

$$w(x) = Ax + B, \tag{2.50}$$

$$v(x) = Cx + D. \tag{2.51}$$

Affes *et al.* (1993) estimated the constants A, B, C and D from the experimental vortex trajectory at points as far as possible from the airframe (approximately 50 core radii or 5 airframe radii a_v). This linear shear model is applied herein.

2.6. *Vortex propagation model*

The vortex is modelled by a piecewise-continuous distribution of finite-length vortex segments terminated by straight, semi-infinite ends parallel to the airframe x-axis. The velocity field generated by each segment is based on the zero-radius model, although a physical radius is assigned to each segment. To calculate the vortex trajectory, the velocities generated locally in the vortex segment and panel coordinates are first transformed into the global vortex-airframe system coordinates. The vortex segment centreline endpoints are then advanced by solving the differential equation:

$$\frac{\mathrm{d}\boldsymbol{x}_v}{\mathrm{d}t} = \boldsymbol{u}_v, \tag{2.52}$$

where $\boldsymbol{x}_v$ is the set of vortex-segment endpoint-position vectors in the global coordinates, t is the time, and $\boldsymbol{u}_v$ is the set of segment endpoint velocity vectors due to all vortex segments, cylindrical airframe source panels and the mean flow. An Adams–Moulton method is used to solve this system of equations. As the vortex moves, the physical core radius for each vortex segment is evaluated. We assume that the core volume of each segment is conserved as the vortex segment stretches or compresses as determined by the motion of the segment endpoints. The helical advance ratio and cutoff parameter of each vortex segment, which are functions of the segment core radius, are then recalculated at each timestep. The cutoff parameter is defined directly from the core radius in (2.35). The helical advance is evaluated through the parameter $\tan^2\beta$ as defined in (2.33) and based on figure 6. The initial value of this parameter is set by comparison to experiment. We note from the equation and figure that $\tan^2\beta$ is proportional to $(b/s)^2$. The quantity b is directly proportional to core radius (a), while s is inversely proportional to a^2 when the segment volume is conserved. From this, we find that $\tan^2\beta$ varies with a^6 as the vortex segment deforms.

When vortex segments of different core radii are joined together to form a model of an extended vortex, it is appropriate to include an annular disk with a distribution of radial vorticity to bridge the segments. The need for this component is readily seen if we consider an initially straight vortex. Stretching the vortex differentially along its length will result in a taper. This taper will induce a component of velocity along the vortex axis that would not exist in a segmented model of the vortex no matter how finely noded. This component of vorticity is not included in the current model because the formulation of the connecting vorticity is complicated when the segments form a curved, rather than straight, vortex. The effect of the neglected vorticity has been evaluated for the axisymmetric case and found to be small compared to the overall azimuthal vorticity given the small degree of vortex taper experienced in this research. This effect is compensated for by adjusting the strength of the azimuthal vorticity through the $\tan^2\beta$ parameter so as to produce the desired axial velocity at the centre of the vortex.

One other practical matter must be considered. The endpoints defining the vortex segments are advected away from the airframe by the axial component of the segment velocity field. To prevent the gridded vortex region from moving laterally away from the airframe, the vortex segments are regridded to their original global x-position after each timestep and the core radius for each segment is then interpolated.

2.7. *Pressure calculation*

Airframe pressure loading is calculated by integrating the Euler equations over the cylindrical surface. The non-dimensionalized axial pressure gradient is given by

$$-\frac{\partial P}{\partial z} = \frac{\partial w_s}{\partial t} + (w_s - c)\frac{\partial w_s}{\partial z} + \frac{v_s}{r}\frac{\partial w_s}{\partial \theta}, \tag{2.53}$$

where w_s and v_s are surface speeds in the axial and azimuthal directions, respectively, and c is the translational speed of the panel mesh. The Euler equation is integrated along z at a constant θ; in particular, the axial derivative is integrated from $z = -L$

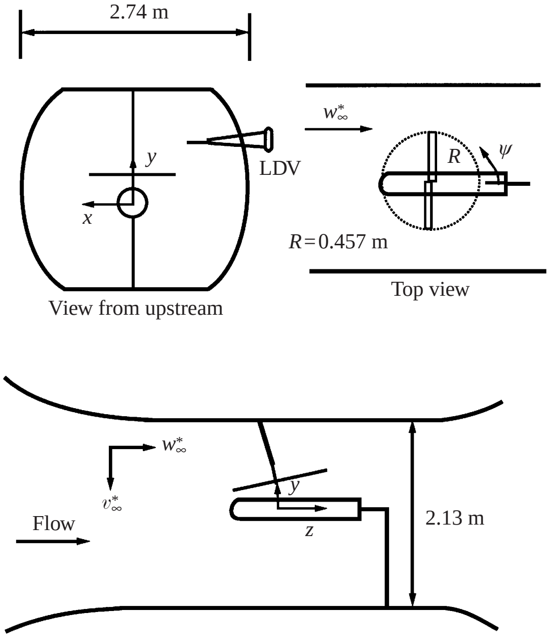

FIGURE 7. The experimental configuration.

to z' analytically to find

$$\int (w_s - c)\frac{\partial w_s}{\partial z} = \tfrac{1}{2}(w_s^2 - w_{s,-L^2}) - c(w_s - w_{s,-L}), \tag{2.54}$$

where

$$w_{s,-L} = w_s(\theta, -L) \tag{2.55}$$

and $2L$ is the length of the computational domain. The time and azimuthal derivatives are evaluated by central differencing and then integrated using the trapezoidal rule. Note that the pressure is referenced to a value of zero away from the airframe. Predicted pressures at both ends of the finite airframe include the effects of the vortex velocity field and are thus consistently negative compared to the reference pressure.

2.8. *Results of the zero-radius helical μ-vortex model*

The numerical model of the zero-radius μ-vortex and airframe were applied to predict the vortex trajectory, vortex core radius and airframe surface pressure resulting from advection of an initially straight axial-flow vortex toward a cylindrical airframe. Initial vortex and airframe parameters were based on the experiments at the Georgia Institute of Technology, as summarized by Kim & Komerath (1995).

The experimental facility consists of a rotor and a cylindrical representation of a helicopter airframe placed in a wind tunnel as shown in figure 7. Significant parameters of the facility as configured for this comparison are

(i) Airframe radius (a^*_R) = 0.067 m,
(ii) Free-stream velocity (w^*_∞) = 10 m s^{-1} at 2100 r.p.m. and
(iii) Rotor advance ratio = 0.1,

where * indicates a dimensional parameter.

For the computations presented here, all parameters were non-dimensionalized on the airframe radius a^*_R and the free-stream mean velocity w^*_∞. Following the illustration in figure 4, the z-axis is oriented along the modelled airframe which has a length of 10. It is represented by 81 axial and 40 azimuthal panels clustered about the top centre of the cylinder with a minimum 0.005 length and 1° width, respectively. The vortex is initiated as a straight, infinite vortex located parallel to the x-axis at $(y, z) = (1.3, 0.0)$. It is represented by 76 finite vortex segments, with a minimum length of 0.005 and cumulative length of 10, plus two semi-infinite end segments. Recently measured values of vortex circulation, core radius and axial velocity (Mahalingam *et al.* 1997) were incorporated into the initial conditions. These average to a circulation $\Gamma^* = 1.0\,\mathrm{m\,s^{-2}}$ or $\Gamma = 1.493$, an initial core radius $a^* = 6.7\,\mathrm{mm}$ or $a = 0.1$, and a vortex axial velocity $u^* = 32\,\mathrm{m\,s^{-1}}$ or $u = 3.2$. We should note that the experimental trajectory and pressure data were taken at a rotor speed of 2100 r.p.m. while other parameters such as circulation and axial velocity have since been refined with measurements at 1050 r.p.m. This is accounted for in the non-dimensionalization by maintaining a constant rotor advance regardless of rotor speed.

The mean velocity field was estimated by Affes *et al.* (1993), who determined that the vortex ends well away from the airframe were advected correctly given

$$w = 1.315 + 0.045x, \tag{2.56}$$

$$v = -0.557 - 0.1245x. \tag{2.57}$$

To evaluate the effect of axial core velocity unambiguously, we wished to advect the vortex toward the airframe as squarely as feasible, without the tilt caused by the shear in the experimental velocity field or the vortex deformation caused by the presence of the airframe. This was accomplished by ignoring shear in the downwash and by artificially increasing the v-velocity near $x = 0$ as described by the expression

$$v = -0.557(1 + A_1 \exp(-|x|/A_2), \tag{2.58}$$

with $A_1 = 0.7$ and $A_2 = 1.0$. This modification causes the vortex to advect nearly linearly across the top of the airframe with an approach speed of the magnitude observed in the experiments.

Once initiated, the vortex is allowed to propagate freely with a typical dimensionless timestep of 0.001. The sensitivity of the results obtained to the number of panel and vortex segments, airframe and vortex length and time increment has been tested. Doubling the number of panels or vortex segments, or increasing the airframe or vortex length, has little effect on the result. Four-digit accuracy is obtained for vortex trajectory and two-digit accuracy is obtained for pressure at the times presented unless otherwise noted. Timesteps are chosen to ensure that vortex movement does not exceed the narrowest panel width in any interval, so timesteps are typically shortened as the vortex approaches the airframe. Decreasing the timestep further has little effect other than to provide finer resolution of the exact time at which a vortex segment endpoint is predicted to penetrate the airframe.

The effects of axial velocity can be demonstrated by comparing cases with no axial velocity, a low velocity of 0.5 and a velocity of 3.2 that corresponds to the experiment. The predicted vortex x-y and x-z trajectories for the case with no axial velocity given the downwash velocity of (2.58) are depicted in figure 8. The imposed downwash velocity advects the vortex in a nearly straight line, although the effects of the airframe are clear. Note that the final vortex position is only a small fraction of the initial vortex core radius from the airframe surface. In the z-direction the head of the vortex is driven toward the front of the airframe by the action of the approaching image vortex, resulting in significant stretching of the centre section of the vortex.

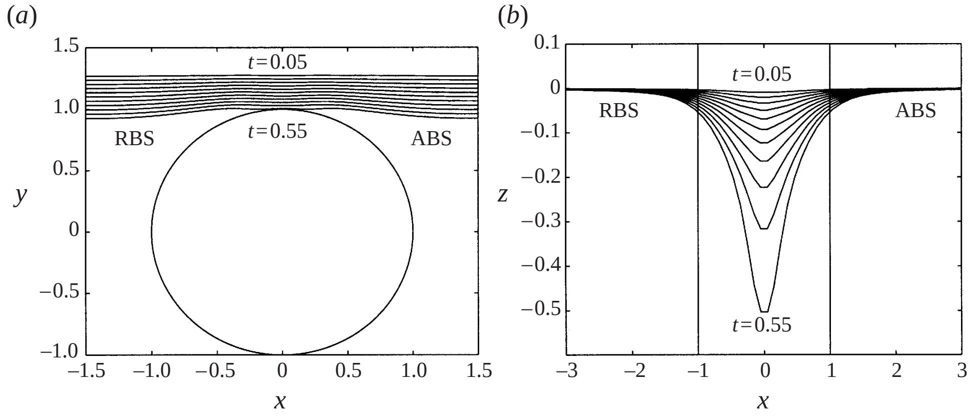

FIGURE 8. Vortex trajectory from $t = 0.05$ to 0.55 in 0.05 increments. (*a*) the (x, y)-plane, (*b*) the (x, z)-plane. The boundary of the airframe is also shown. Note that the x-scales are different to best show the details of the trajectory.

Vortex core radius for three axial velocity cases are presented in figure 9. With no axial velocity, in figure 9(*a*), the core radius is observed to thin symmetrically as the vortex approaches the airframe. This thinning accelerates as the vortex stretches into an elongating horseshoe, as seen in figure 8(*b*). Previous results for μ-vortex models (Affes *et al.* 1993, Radcliff *et al.* 1997) demonstrate similar behaviour.

Invoking a relatively small vortex axial velocity of 0.5 ($5\,\mathrm{m\,s^{-1}}$) causes some asymmetry in the core radius, as shown in figure 9(*b*). Compared with the case of zero axial velocity, the core radius is thinning on the retreating blade side of the airframe and dilating on the advancing blade side. The thinning is notable from just off the airframe centreline to several airframe radii away, indicating an outward advective effect due to the vortex axial velocity. Vortex core dilation shows an inward advective effect, with dilation becoming localized near $x = 0$ where the legs of the vortex nearly parallel the airframe axis. Also, the overall magnitude of the thinning, which is greatest just above the airframe, is less than for the previous case.

Increasing axial velocity to 3.2 ($32\,\mathrm{m\,s^{-1}}$), the magnitude experienced in experiments, results in a dramatic extension of the trends observed at low axial velocity. Core radius, as shown in figure 9(*c*), presents significantly more asymmetry. Thinning on the RBS, advected well away from the point of close interaction by the higher axial velocity, extends much further from the airframe, while the core dilation is advected closer to the airframe centreline ($x = 0$). More striking is the magnitude of the thinning and dilation, which is much smaller than before. The maximum thinning observed, now slightly to the RBS side of the airframe centre, is only of the order of 10%, where it was nearer to 50% in previous cases. Stretching of the vortex, indicated by the (x, z)-trajectory shown in figure 10, is reduced by perhaps 30% when compared with the zero velocity result in figure 8(*b*). Although the trajectory still appears substantially symmetric, all of the vortex stretching now occurs on the RBS side of the airframe, whereas stretching is symmetric about $x = 0$ in figure 8(*b*).

The surface pressure along the top of the airframe ($x = 0$) is shown in figure 11 for the different axial velocity cases. With no axial velocity, shown in figure 11(*a*), the constant-circulation vortex thins, the azimuthal vorticity increases and the pressure predicted along the top of the airframe cylinder shows a steadily deepening suction peak directly below the approaching vortex. This is in agreement with previous results

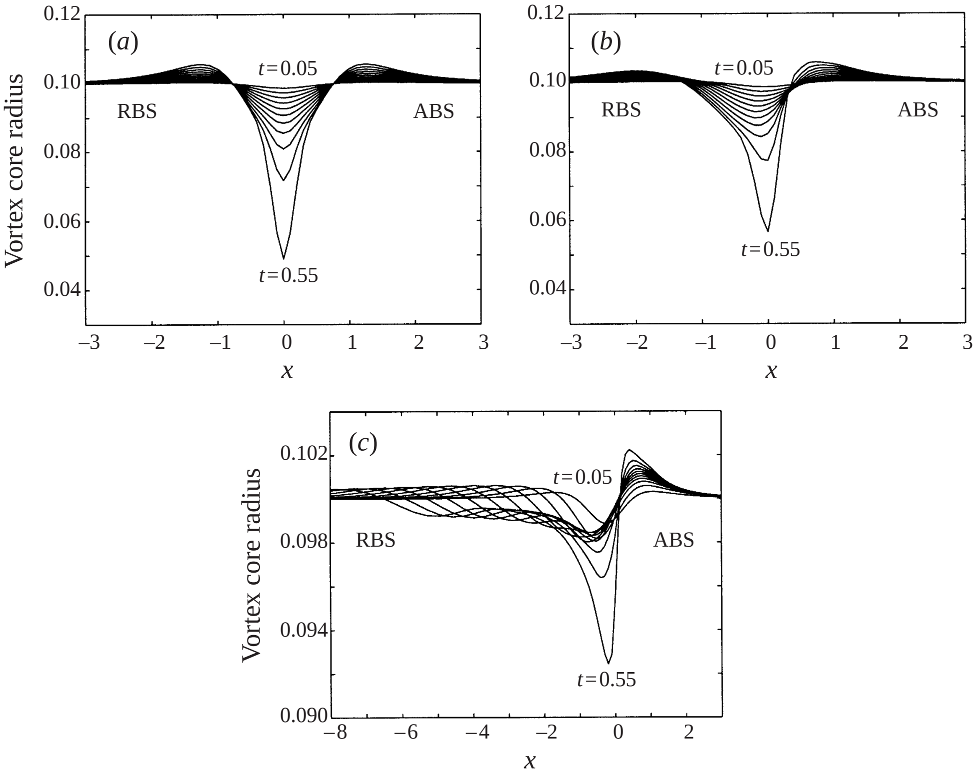

FIGURE 9. Vortex core radius from $t = 0.05$ to 0.55. (*a*) No vortex core axial velocity; (*b*) axial velocity of 0.5 within the vortex core; (*c*) axial velocity of 3.2 within the vortex core.

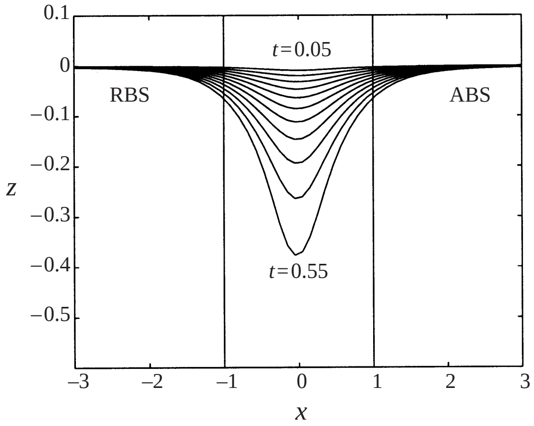

FIGURE 10. Vortex trajectory from $t = 0.05$ to 0.55 with a vortex core axial velocity of 3.2.

(Affes *et al.* 1993). Note that the pressure integrated along the airframe surface does not return to the intial value, with increasing error as time advances. For this reason, the pressure results are not presented past $t = 0.50$. The cause of this error is discussed in the next section where an upgraded vortex model is introduced.

The surface pressure resulting from an axial velocity of 0.5 is shown in figure 11(*b*). On direct comparison with the zero axial velocity case, we can see that the magnitude

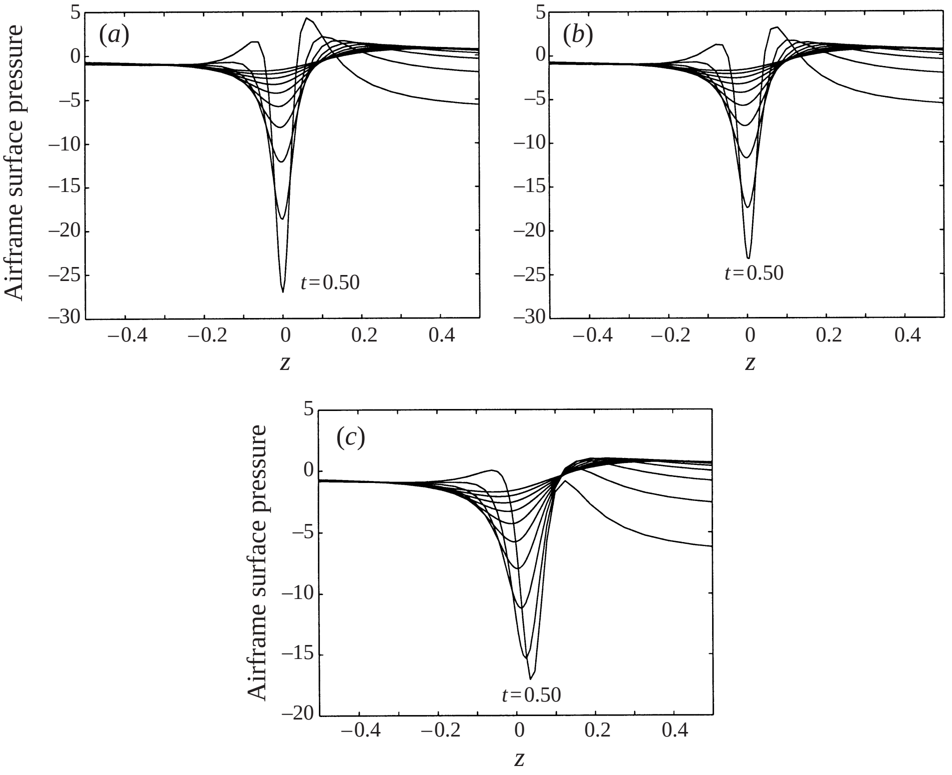

FIGURE 11. Airframe surface pressure at $x = 0$ induced by the approaching vortex from $t = 0.05$ to 0.50. (*a*) No vortex core axial velocity; (*b*) axial velocity of 0.5 within the vortex core; (*c*) axial velocity of 3.2 within the vortex core.

of the suction peak at $z = 0$, although still increasing with time, shows some sign of slowing as axial velocity is increased. The pressure fails to recover at large z in the same manner as the zero axial velocity case.

These trends continue when axial velocity is increased to 3.2, as shown in figure 11(*c*). Until $t = 0.45$, the suction peak is only slightly less than in the previous cases, but, with high axial velocity, the increase in magnitude of the peak is nearly stopped by $t = 0.5$. A closer look at the pressure from $t = 0.45$ to 0.55 is given in figure 12. We can see that the suction peak actually reverses after $t = 0.5$, a behaviour exhibited in experiments, although the continued lack of pressure recovery at large z casts doubt on the result.

Summarizing, in the case of no axial velocity we see the image vortex forcing the vortex head toward the front of the airframe, stretching the vortex symmetrically about the airframe axis. This stretching reduces the core radius and thus increases vorticity and swirl velocity locally. The increase in swirl then reinforces the vortex head motion, a feedback effect that results in continued stretching and thinning. The final result is an ever-growing suction peak on the top of the airframe, a prediction not supported by experiment.

As axial velocity is increased, advection causes strong asymmetry about the airframe along the x-axis. The image vortex still acts to force vortex head motion, but stretching of the vortex is inhibited by the effects of axial velocity. As the vortex stretches, the alignment of the vorticity changes to increase the axial vorticity component at the

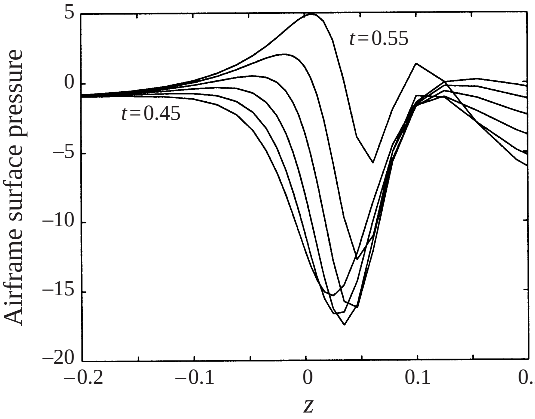

FIGURE 12. Airframe surface pressure at $x = 0$ from $t = 0.45$ to 0.55 in increments of 0.02. Axial velocity within the vortex core is 3.2.

expense of the azimuthal component, as is clear from the illustration of the helical vortex in figure 6. This means that vortex segment stretching initiated by the image vortex causes a reduction in the vortex core axial velocity, which then limits the stretching of the segment. The opposite is true in the case of vortex dilation. It would be expected that this action would inhibit the z-direction movement of the vortex, and, in fact, some reduction in motion is seen when comparing figures 8(*b*) and 10. However, the core radius depicted in figure 9(*c*) demonstrates that vortex stretching, rather than occurring in a symmetric manner directly over the airframe, now occurs completely on the retreating blade side of the airframe and over a much longer distance as the slightly thinned vortex is advected away from the region of closest interaction. Although the vortex trajectory is relatively unaffected, the thinning of the vortex is reduced in magnitude while increased in coverage. The feedback effect is thus avoided and airframe surface pressure is seen to reach a minimum and consequently reverse as observed in experiments. However, the failure of the predicted pressure to recover to its initial value casts doubt on this observation.

3. Deformable core axial-flow vortex

Considering the position of the edge of the vortex core relative to the airframe suggests a hypothesis for the observed anomaly in pressure. In the present model, each helical vortex segment is represented by a single line of μ-distributed axial vorticity surrounded by distributed azimuthal vorticity. The position of the vortex segment is determined by its centreline endpoints. Surface pressure in the model is calculated by starting with a known pressure, well away from the vortex, and then integrating the Euler equation along a line on the airframe surface that passes under or through the vortex. As the vortex approaches the surface, the pressure at the end of the line of integration beyond the vortex is not observed to return to the initial value as expected, but rather is increasingly underpredicted.

The first time at which pressure fails to recover fully is $t = 0.3$ in figure 11(*a*). Referring to the trajectory and radius figures, we note that the distance between the vortex and the airframe at $x = 0$ becomes less than the vortex core radius after $t = 0.25$. Although the panel model of the airframe enforces a zero-normal-velocity boundary condition at the airframe surface, nothing prevents the distributed axial

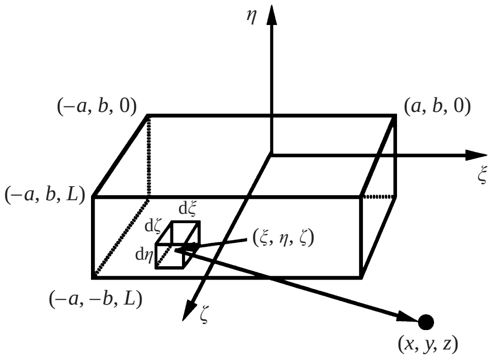

FIGURE 13. Box-vortex segment configuration.

vorticity from unphysically overlapping the space occupied by the solid airframe as the vortex centreline advects to within a core radius. This is believed to be the cause of the observed pressure anomaly. Further support of this hypothesis is gained by studying the cases with increased axial velocity. When axial velocity is 0.5, the core radius directly above the airframe changes little from the zero axial velocity case, as does the magnitude of the pressure anomaly. When the velocity is increased to 3.2, the core radius decreases much less and the observed magnitude of the anomaly after $t = 0.3$ increases as more vorticity overlaps the airframe.

To circumvent this problem, a model in which vorticity is maintained within a bounded region that cannot cross solid boundaries was formulated. Observations of experimental vortex–surface collisions show the vortex core flattening into an ellipse before the vortex merges into the boundary layer. However, the mathematics of bounded vorticity within an ellipse are quite complicated, so we have applied a rectangular, or 'box' vortex formulation. In this box-vortex model, axial and azimuthal components of vorticity are distributed uniformly over the interior of a rectangular core volume. This distribution of vorticity prevents the singularity in velocity at the core boundary that the cutoff parameter μ was originally introduced to avoid, so μ is not used in the box-vortex model and thus all vorticity is enclosed within the vortex boundary. Variation of the aspect ratio of this box-vortex core maintains the vorticity outside of the airframe on close approach while still preserving the calculated vortex cross-sectional area. The derivation, which was presented previously by Radcliff *et al.* (1999), is repeated here for completeness.

3.1. *The box-vortex velocity field*

The three-dimensional velocity field that results from a finite-length rectangular vortex segment with distributed vorticity is found by defining a uniform distribution of line vortices oriented along each of the box-vortex coordinate axes and then integrating each orthogonal velocity component induced over the volume of the rectangular box-vortex segment. The velocity field for each line vortex in the distribution is again given by the Biot-Savart law, equation (2.1). The integration for each velocity component in each coordinate is similar if the appropriate order of integration is chosen, so only the integration of a typical component of the axial vorticity distribution is presented here.

We start with a differential vortex element located at the point (ξ, η, ζ) within a finite box vortex segment, as shown in figure 13. Cartesian coordinates originate at the end of the segment with the ζ-axis parallel to the axis of the box-vortex, thus transposing the local ξ and ζ axes compared with the local x and z axes of the cylindrical vortex formulation of figure 5. To evaluate the velocity induced at a field point (x, y, z) by axial vorticity ω uniformly distributed over a rectangular volume, we represent the circulation vector by $\mathrm{d}\boldsymbol{\Gamma} = \boldsymbol{k}\, \omega\, \mathrm{d}\xi\, \mathrm{d}\eta\, \mathrm{d}\zeta$. Thus, the non-zero components of velocity are

$$\mathrm{d}u'' = -\frac{\omega\, \mathrm{d}\xi\, \mathrm{d}\eta\, \mathrm{d}\zeta}{4\pi} \frac{y-\eta}{r^3}, \tag{3.1}$$

and

$$\mathrm{d}v'' = \frac{\omega\, \mathrm{d}\xi\, \mathrm{d}\eta\, \mathrm{d}\zeta}{4\pi} \frac{x-\xi}{r^3}, \tag{3.2}$$

where $r = \sqrt{R^2 + (z-\zeta)^2}$, and R is the perpendicular radius $R = \sqrt{(x-\xi)^2 + (y-\eta)^2}$.

Integrating the differential vortex element into a vortex line segment of finite length $\zeta = 0$ to L, we find the u-component of velocity by integration with respect to ζ as

$$\mathrm{d}u' = -\frac{\omega\, \mathrm{d}\xi\, \mathrm{d}\eta}{4\pi}(y-\eta) \int_0^L \frac{\mathrm{d}\zeta}{[R^2 + (z-\zeta)^2]^{3/2}}. \tag{3.3}$$

Thus, for the vortex segment

$$\mathrm{d}u' = \frac{\omega\, \mathrm{d}\xi\, \mathrm{d}\eta (y-\eta)}{4\pi R^2} \left[\frac{z-L}{\sqrt{R^2 + (z-L)^2}} - \frac{z}{\sqrt{R^2 + z^2}} \right]. \tag{3.4}$$

Next, a vortex sheet is formed by integrating the segments with respect to η over the range $-b < \eta < b$ to find

$$\mathrm{d}u = \frac{\omega\, \mathrm{d}\xi}{4\pi} \left[(z-L) \int_{-b}^{b} \frac{(y-\eta)\, \mathrm{d}\eta}{R^2 \sqrt{R^2 + (z-L)^2}} - z \int_{-b}^{b} \frac{(y-\eta)\, \mathrm{d}\eta}{R^2 \sqrt{R^2 + z^2}} \right]. \tag{3.5}$$

It is convenient to introduce $t = R^2 = (x-\xi)^2 + (y-\eta)^2$, such that the integrals in the above formula simplify to

$$\mathrm{d}u = \frac{\omega\, \mathrm{d}\xi}{8\pi} \left[z \int_{\eta=-b}^{\eta=b} \frac{\mathrm{d}t}{t\sqrt{t + z^2}} - (z-L) \int_{\eta=-b}^{\eta=b} \frac{\mathrm{d}t}{t\sqrt{t + (z-L)^2}} \right]. \tag{3.6}$$

With the result

$$\begin{aligned} \mathrm{d}u = \frac{\omega\, \mathrm{d}\xi}{4\pi} & \left[\ln\left(\frac{\sqrt{(\xi-x)^2 + (b-y)^2 + z^2} - z}{\sqrt{(\xi-x)^2 + (b+y)^2 + z^2} - z} \right) \right. \\ & \left. - \ln\left(\frac{\sqrt{(\xi-x)^2 + (b-y)^2 + (z-L)^2} - (z-L)}{\sqrt{(\xi-x)^2 + (b+y)^2 + (z-L)^2} - (z-L)} \right) \right]. \end{aligned} \tag{3.7}$$

Now we form a rectangular volume of uniform vorticity by integrating the vortex sheet with respect to ξ over the range $-a < \xi < a$. Hence, from (3.7), we need to evaluate integrals of the form

$$I(s) = \int \ln\left(\sqrt{s^2 + \alpha^2 + \beta^2} - \beta \right) \mathrm{d}s. \tag{3.8}$$

Evaluating the indefinite integral yields

$$\begin{aligned} I(s) = {} & s \ln\left(\sqrt{s^2 + \alpha^2 + \beta^2} - \beta \right) - s - \beta\, \mathrm{sgn}\,(s) \ln\left(|s| + \sqrt{s^2 + \alpha^2 + \beta^2} \right) \\ & + \alpha \arctan\left(\alpha s / [\alpha^2 + \beta^2 - \beta\sqrt{s^2 + \alpha^2 + \beta^2}] \right). \end{aligned} \tag{3.9}$$

Finally, reverting back to the original x, y, z variables, the elemental integrals of the log-factors in (3.7) may be written as

$$\int_{-a}^{a} \ln\left(\sqrt{(\xi - x)^2 + (b+y)^2 + (z-L)^2} - (z-L)\right) \mathrm{d}\xi$$
$$= \mathscr{F}(a-x, b+y, z-L) - \mathscr{F}(-a-x, b+y, z-L), \qquad (3.10)$$

where the $\mathscr{F}$-function is defined as

$$\begin{aligned} \mathscr{F}(x,y,z) = {} & x \ln\left(\sqrt{x^2+y^2+z^2} - z\right) \\ & - y \arctan\left(\frac{xy}{y^2+z^2-z\sqrt{x^2+y^2+z^2}}\right) \\ & + z \,\mathrm{sgn}\,(x)\left[\ln\left(|x| + \sqrt{x^2+y^2+z^2}\right) - \ln\sqrt{y^2+z^2}\right]. \end{aligned} \qquad (3.11)$$

Adapting (3.10) to match the various log-factors in (3.7), the ξ-component of velocity induced by axial vorticity uniformly distributed throughout a rectangular volume is given by

$$\begin{aligned} u = \frac{\omega}{4\pi} [& \mathscr{F}(a-x, b-y, z) - \mathscr{F}(-a-x, b-y, z) \\ & + \mathscr{F}(a-x, b+y, z-L) - \mathscr{F}(-a-x, b+y, z-L) \\ & - \mathscr{F}(a-x, b-y, z-L) + \mathscr{F}(-a-x, b-y, z-L) \\ & - \mathscr{F}(a-x, b+y, z) + \mathscr{F}(-a-x, b+y, z)]. \end{aligned} \qquad (3.12)$$

The velocity components from vorticity distributed parallel to the ξ- and η-axes of the box-vortex are solved in the same manner. For vorticity component ω_η, we will find the u- and w-components of velocity by integrating in the order η, ζ, ξ and η, ξ, ζ, respectively, while the v- and w-components from vorticity component ω_ξ can be found by integrating over ξ, ζ, η and ξ, η, ζ, respectively. Note that, in each case, the sign of the vorticity will change at the centre of the box vortex so these velocity expressions will have twice the number of $\mathscr{F}$-function evaluations as that shown in (3.12).

The uniform distribution of the vorticity components ω_η and ω_ξ in each quadrant of the (η, ξ)-plane corresponds to a resultant vorticity distribution in the form of diamond-shaped vortex loops over the interior of the box. For completeness, the vortex loops that intersect the edges of the box must be closed by vortex segments lying along these edges. Our experience has shown that concentration of vorticity on the edges of the vortex segment cross-section can lead to instability in the advection of neighbouring vortex segments that make up the tip-vortex model. For this reason, the present model does not include the connecting vortex segments along the edge of the box. In addition, the vorticity distribution that connects the vortex segments has been neglected, as discussed in §2.6. Both effects have been compensated for by adjusting the strength of the interior vorticity so as to produce the desired axial velocity at the centre of the vortex.

3.2. *Incorporating the box vortex into the interaction model*

To incorporate the box-vortex velocity field expressions with the rest of the numerical vortex–surface interaction model previously described in §§ 2.4 to 2.7, two additions are required. First, variation of the aspect ratio of the vortex must be modelled. The vortex propagation model of § 2.6 evaluates the radius and therefore area of the cylindrical vortex core through conservation of vortex segment volume. For the box vortex, this area is evaluated as an effective core radius such that $\pi a_{eff}^2 = 4ab$. The box-vortex core is initially represented by a square cross-section with an aspect ratio (b/a) of unity. As the vortex stretches and the cross-sectional area decreases, a and b decrease equally until the vortex segment centreline and airframe surface are separated by less than the effective core radius. Then, b is set equal to the separation distance to prevent vorticity from overlapping the airframe, while a is increased to maintain the original vortex segment cross-sectional area. Deformation of the vortex (η, ξ)-cross-section will cause a change in the areas of the (η, ζ)- and (ξ, ζ)-planes of the deformed segment, so the azimuthal vorticity components must be modified to correct for this. This is accomplished by multiplying ω_η by a_0/a and ω_ξ by b_0/b, where a_0 and b_0 are the initial box vortex core dimensions corrected for vortex stretching, while a and b are the core dimensions predicted at the current time by the vortex deformation model.

Next, the direction of the local vortex-segment coordinates relative to the global coordinates must be specified carefully. When calculating the global model velocity field, the contribution of each vortex segment must be transformed from segment local coordinates of figure 13 to the global airframe coordinates of figure 4. When the axisymmetric helical vortex model was used, the transformation from the vortex segment coordinates to the global coordinates required two rotations, the rotation of the segment about the vortex axis being immaterial. With the box-vortex model, a third rotation must be defined to keep the segment (ξ, ζ)-plane tangential to the closest airframe point, ensuring that the vortex segment flattens against, rather than into, the airframe surface. This was accomplished through the initial definition of the vortex segment basis vectors. The segment axis basis $\hat{e}_\zeta$ is defined in both models by the endpoints of the vortex segment centreline that are tracked by the Lagrangian advection model. Basis vector $\hat{e}_\eta$ can then be defined normal to the cylindrical airframe surface by setting the component of $\hat{e}_\eta$ in the axial (z) direction of the airframe equal to zero (i.e. $\hat{e}_\eta = a_{\eta\zeta}\hat{i} + a_{\eta\eta}\hat{j}$) and letting $\hat{e}_\zeta \cdot \hat{e}_\eta = 0$. Finally, basis $\hat{e}_\xi$ is given by $\hat{e}_\zeta \times \hat{e}_\eta$. This combination of vortex flattening and coordinate basis ensures vorticity will not overlap the airframe until the vortex centreline violates the surface.

3.3. *Results of the revised model*

In this section we present effective core radius and airframe surface pressure for the zero and non-zero axial velocity cases studied previously with the helical vortex model. With the obvious exception of an initially square cross-section vortex, the vortex and airframe parameters are maintained and the figures are directly comparable to those presented previously.

The effective core radius, core aspect ratio and surface pressure for the case with no axial velocity are presented in figure 14. Here, the total vortex segment cross-sectional area is represented by the effective core radius defined above and the aspect ratio is defined as vortex core height (normal to the airframe) divided by the core width. The effective core radius is very similar to that predicted with the helical vortex model, figure 9(*a*), until after $t = 0.45$. After this time, the core radius in the box-vortex

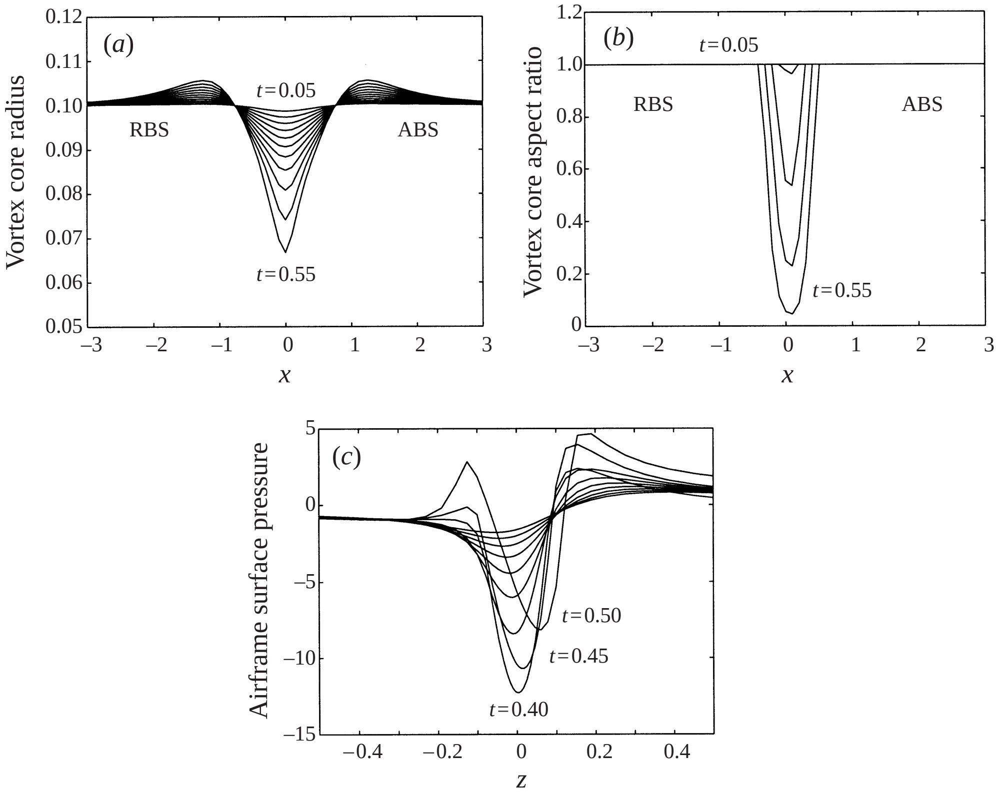

FIGURE 14. (*a*) Vortex core effective radius ($\pi a_{eff}^2 = 4ab$), and (*b*) core aspect ratio b/a from $t = 0.05$ to 0.55; and (*c*) airframe surface pressure from $t = 0.05$ to 0.5, in increments of 0.05. All predictions apply the box-vortex formulation. Note that the aspect ratio is unity until after $t = 0.35$. Axial velocity within the vortex core is zero.

model decreases at a much slower rate than in the previous prediction. Deformation of the vortex core is the probable reason as a significant portion of the vortex flattens by more than half after $t = 0.45$, with a deformation as large as $25:1$ at $t = 0.55$. The z-direction trajectory of the vortex head (not shown) is also noted to slow after $t = 0.45$, presumably for the same reason, otherwise the trajectory is similar to that predicted by the helical vortex model.

The effects of core deformation are clear in the surface pressure prediction. Unlike the prediction of the helical vortex model in figure 11(*a*), where suction strengthens until the end time of $t = 0.5$, surface suction predicted with the box-vortex model increases only until $t = 0.4$ and then begins to decrease. Because of this, the peak suction is of the order of 12, a smaller value than was observed in any of the cases evaluated using the helical vortex model. Also notable is that pressure now recovers to the original value away from the vortex. Although a small discrepancy is still seen at $t = 0.4$, when the suction peak begins to recover, the improvement from using the box-vortex formulation is clear. Pressure recovery errors do occur after $t = 0.5$, but the magnitude of the errors is irregular in value and sign as compared with the monotonic increase seen in figure 11. This is thought to indicate the limit of accuracy in the source-panel velocity calculation.

Applying an axial velocity of 3.2 using the box-vortex model confirms the results of the helical μ-vortex model. Core radius, shown in figure 15(*a*), behaves similarly to

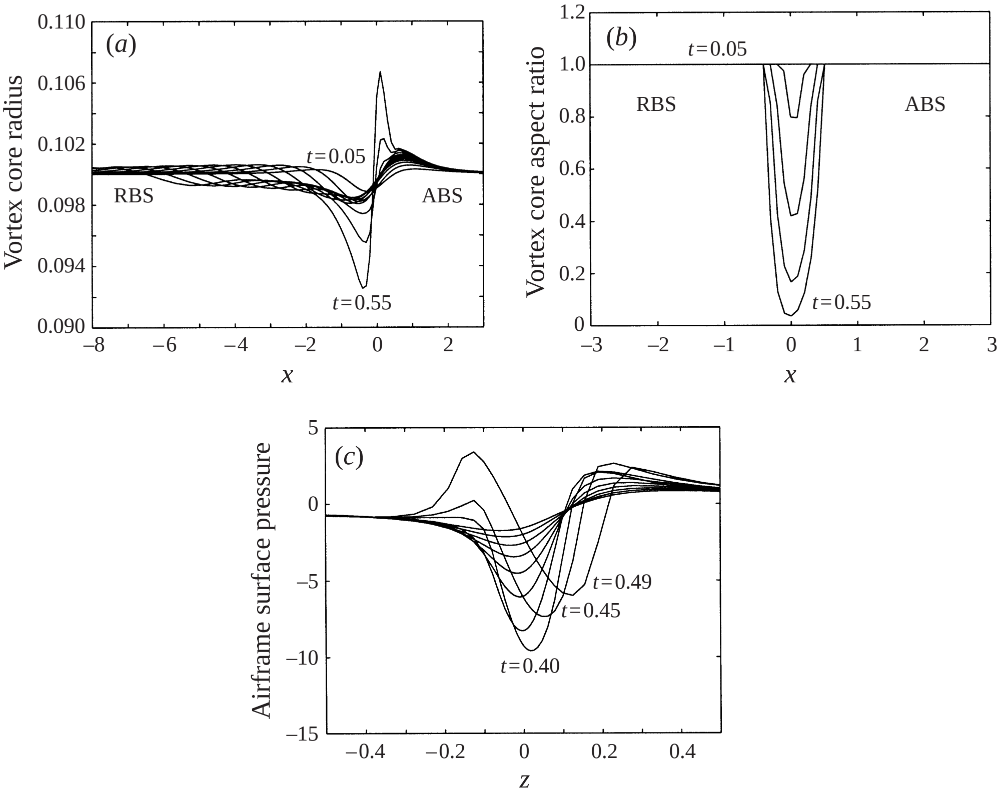

FIGURE 15. (*a*) Vortex core effective radius, and (*b*) core aspect ratio from $t = 0.05$ to 0.55; and (*c*) airframe surface pressure from $t = 0.05$ to 0.5. Axial velocity in the vortex core is 3.2.

the comparable result in figure 9(*c*). The only notable difference is that significantly more dilation is observed close to the airframe after $t = 0.45$. The associated core aspect ratio in figure 15(*b*) shows little change from the zero axial velocity case, with a slightly broader region of deformed vortex segments. Finally, the airframe surface pressure shown in figure 15(*c*) is similar to that predicted by the box-vortex model with no axial velocity in figure 14(*c*). A notable exception is an increased positive pressure upstream ($z = -0.15$) of the vortex position at $t = 0.49$, the last timestep without significant pressure recovery error. Like the prediction of the helical vortex model, the magnitude of the suction peak is observed to decrease slightly, in this case from -13 to -10, as axial velocity is increased.

Overall, we can see that axial velocity acts to distribute vortex stretching over a considerable distance along the vortex axis, away from the primary interaction point at $x = 0$, causing reversal of the suction peak as seen in experiments. Deformation of the core, a necessary condition for a successful prediction of the airframe surface pressure, also distributes vorticity away from the primary interaction point at $z = 0$, in this case along the airframe axis through vortex flattening, and thus also contributes to the behaviour observed in experiments.

4. Comparison of the box-vortex model with experimental data

The intent of the comparisons presented in the last two sections was to illustrate the effects of axial velocity and vortex core flattening with a vortex, having characteristics

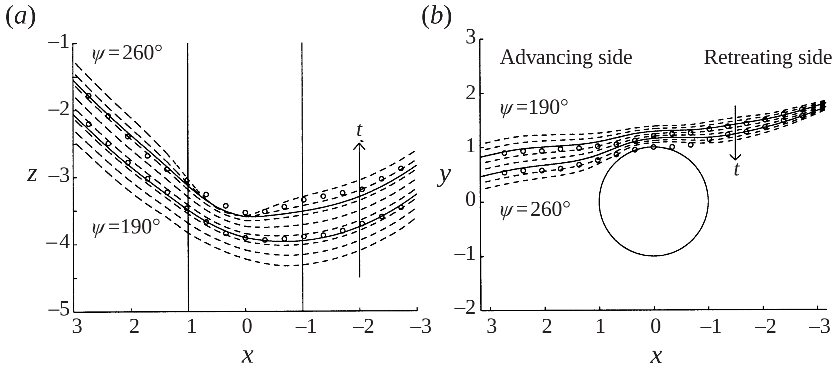

FIGURE 16. Vortex trajectory from $\psi = 190°$ to $260°$. —, computed trajectories at $\psi = 210°$ and $240°$, ○, experimental data at the same times. The initial vortex parameters were specified from experimental observations at $\psi = 180°$. Arrows denote increasing ψ.

similar to those measured in experiments. To improve the clarity of the results, the vortex was maintained unrealistically straight while it was advected into the airframe. To predict the experimental results of Kim & Komerath (1995) and Mahalingham *et al.* (1997) using the box-vortex model, it is only necessary to restore the mean velocity field described by (2.57) and to initiate the vortex segment trajectories from a position defined by the experimental visualization. We started the trajectory at a rotor phase angle ψ of 180°, which gives a minimum vortex–airframe separation of four core radii. The vortex is then allowed to propagate freely under the constraints of the vortex propagation model. A dimensionless timestep of 0.0002388 was applied, corresponding to an advance in rotor phase angle of 0.02°, although a much larger timestep may be used until deformation of the vortex cross-section begins. The simulation is continued until a vortex segment endpoint is predicted to penetrate the airframe surface. Vortex trajectory, strength, core radius, axial velocity and airframe surface pressure are experimental parameters available for comparison.

The predicted vortex trajectory from $\psi = 190°$ to $260°$ is shown in figure 16, along with the measured trajectory from Liou *et al.* (1990) at $\psi = 210°$ and $240°$. The coordinates are the global coordinates shown in figure 4. The trajectory matches well in the (x, z)-plane but we see that the physical vortex moves toward the cylinder more rapidly than the modelled vortex near the centreline of the airframe. These results compare favorably with the simulation of Affes *et al.* (1993), showing that axial velocity has little effect on vortex advection during this time interval.

The prediction shows that the modelled vortex is approaching the airframe more slowly than the physical vortex. In figure 16(*b*), we see that the endpoints of the experimental and numerical vortex trajectories coincide, while the points closer to the cylinder do not. Increasing the magnitude of the downwash velocity in the numerical model allows us to predict the midpoints, but then the endpoints no longer match. This suggests that the linear-shear downwash velocity model in (2.51) is too simple. Indeed, measurements immediately below the rotor but away from the airframe (Liou *et al.* 1990) suggest that the v-velocity directly above the airframe may be more than 50% greater than that at the vortex endpoints.

To test our hypothesis, we developed a model to give a higher-order fit to the downwash velocity. This is reasonable because we are not trying to predict the downwash but simply use it as a boundary condition. The fit of downwash velocity

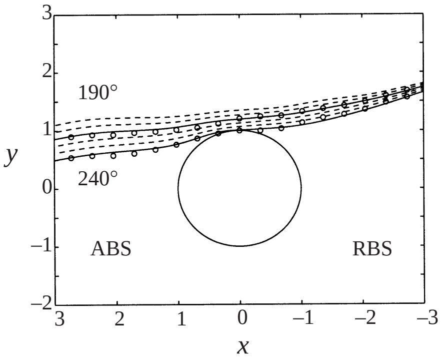

FIGURE 17. Predicted trajectory of the box-vortex with the revised downwash model from $\psi = 190°$ to 240°. ○, experimental data at $\psi = 210°$ and 240°.

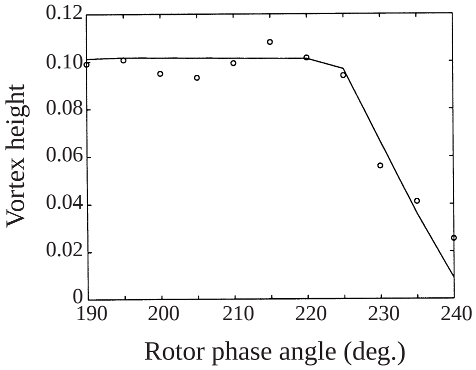

FIGURE 18. Vortex core height directly above the airframe ($x = 0$) as the vortex approaches the airframe surface. ○, Experimental data.

from (2.57) was modified to give

$$v = -0.557(1 + A_1 \exp(-|x|/A_2) - 0.1245x, \tag{4.1}$$

where A_1 and A_2 are adjustable parameters. Through trial and error, these parameters were set to 0.7 and 1.0, respectively, to give the best fit to the positional data. Although there is no direct connection, it may be noted that this downwash model also served to advect the straight vortex in a uniform manner near the airframe in the comparisons presented previously. The resulting trajectory is seen in figure 17. Note that comparison of all predicted results, including core radius, axial velocity and surface pressure, were performed with the downwash models of (2.57) and (4.1). Modifying the downwash distribution changes the timing, but not the magnitude of the predictions. The revised downwash velocity profile is thus applied to compare the model predictions with the experimental data.

Figure 18 shows the comparison of experimental vortex core height (the minor axis of the visualized core as it deforms into an ellipse) from Mahalingam *et al.* (1997) with the numerical predictions of the box-vortex-core height b at $x = 0$.

The comparison of surface pressure on top of the airframe is shown in figures 19 and 20. These figures reflect two sets of data from the same experimental facility, that of Brand (1989) and of Kim & Komerath (1995), respectively. The surface pressures 15° from the top of the airframe to the advancing and retreating blade sides of the

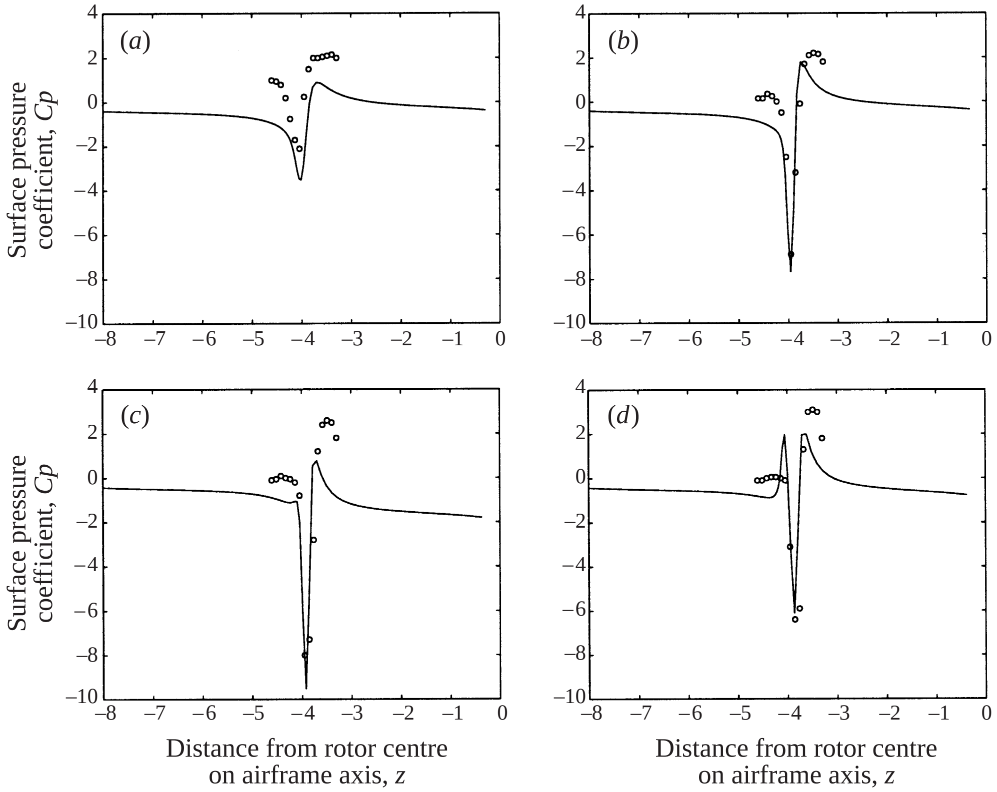

FIGURE 19. Pressure on the airframe surface directly above the airframe centreline as the vortex approaches: (*a*) Rotor phase angle $\psi = 210°$; (*b*) $\psi = 222°$; (*c*) $\psi = 228°$; (*d*) $\psi = 234°$. ○, Brand's (1989) experimental data.

airframe are shown in figures 21 and 22, respectively. The experimental data are those of Kim because Brand did not take pressure data on the sides of the airframe.

These results demonstrate substantially better prediction of the actual interaction than has been previously accomplished (Mahalingam *et al.* 1997). The trends and timing of the comparisons are quite reasonable. Core height predictions agree very well with the experimental observations. Axial velocity values (not shown), do not agree as well, with the experimental values stagnating earlier. However, these are very difficult measurements to obtain, especially as the vortex core thins, because there is a deficit of the reflective particles needed for the optical measurements in the core region.

The surface pressure coefficient shows excellent agreement on top of the airframe. Comparing with Brand's data in figure 19, both strengthening and weakening of the suction peak is predicted with good accuracy considering that the presence of blade passage effects in the experimental data are not modelled numerically. From the comparison with Kim's data in figure 20, we see that the magnitude of the suction peak is somewhat less that that seen in the simulation or in Brand's earlier measurements. This may be explained by the use of Brand's trajectory data to develop the downwash profile given in (4.1). Kim did not repeat the trajectory measurements, so there may be small differences in trajectory that could relate to significant differences in pressure. Pressure recovery errors in the numerical results prevented prediction of experimental results at rotor phase angles larger than those presented.

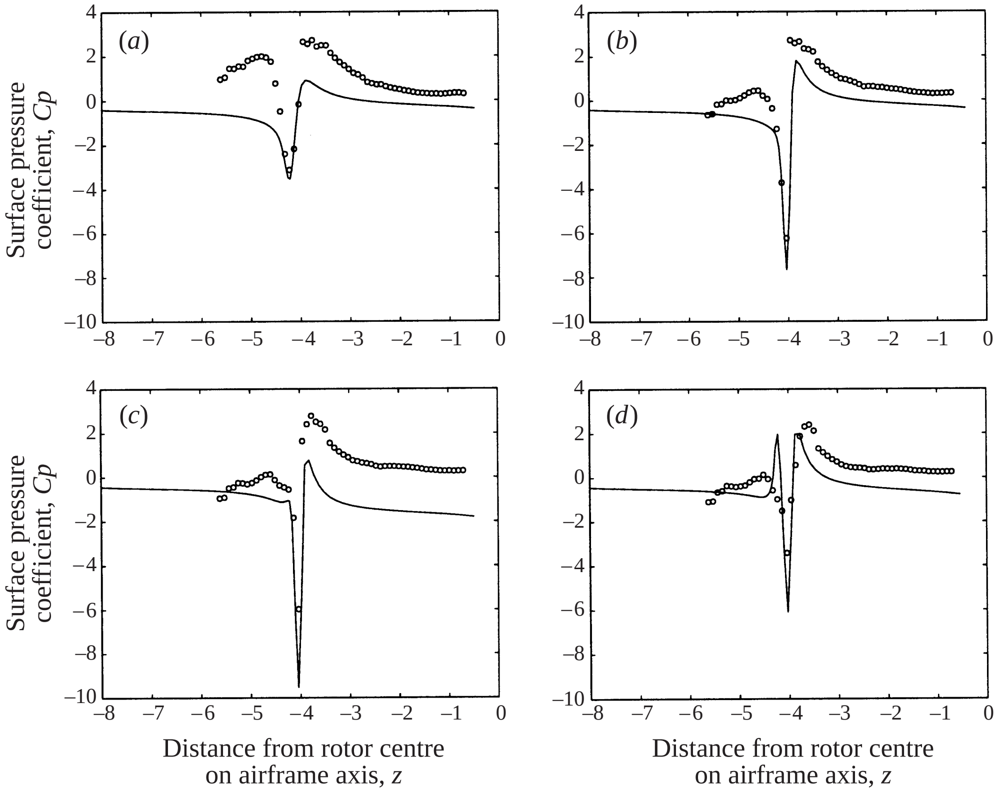

FIGURE 20. Pressure on the airframe surface directly above the airframe centreline as the vortex approaches: (*a*) Rotor phase angle $\psi = 210°$; (*b*) $\psi = 222°$; (*c*) $\psi = 228°$; (*d*) $\psi = 234°$. ○, Kim's (1995) experimental data.

A notable discrepancy in the comparison of experimental and numerical results is the z-position of the suction peaks, which differ by as much as several core radii. This discrepancy was also noted in the results of Affes *et al.* (1993) who used the same data. Study of the results shows that the numerical model predicts the suction peak directly below the vortex position, as would be expected, while in the experiments, the suction peak is systematically displaced by about two core radii from the visualized vortex core at all rotor phase angles. Discussion with the experimenter (Brand 1999 private communication) suggests that this small error has inadvertently arisen from a translation of the pressure sensors, a technique used to obtain pressure data more closely spaced than the actual sensors. For this reason the shift has been removed and this is reflected in the results presented in figures 19–22.

The surface pressures 15° from the top of the airframe to the advancing blade and retreating blade sides, shown in figures 21 and 22, respectively, illustrate the fundamental asymmetry of the pressure field. The trends of the pressure and most of the magnitudes are in fair agreement. On the advancing blade side, suction increases up to $\psi = 234°$, indicating that the vortex is still stretching at this location. On the retreating blade side, the numerical prediction peaks and withdraws by $\psi = 234°$, while the experimental data suggest that a reversal is just beginning. The magnitude of the numerical prediction of the suction peak is substantially larger than the measured value at most of the rotor phase angles on both sides of the airframe, as it is in the

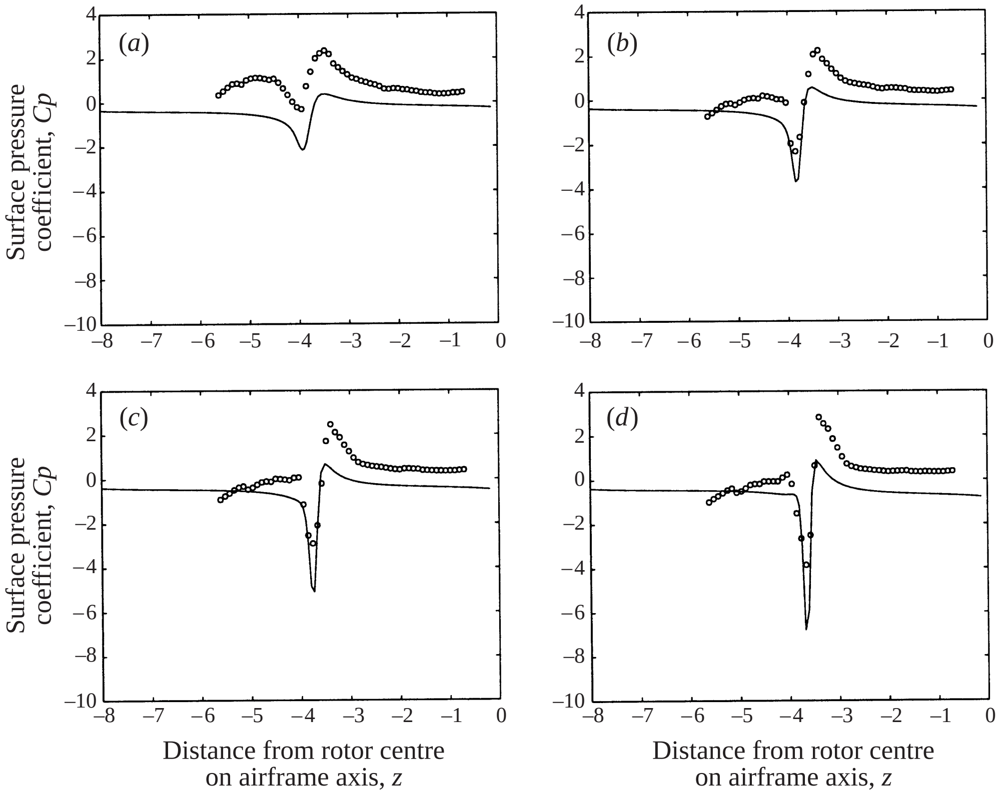

FIGURE 21. Pressure on the airframe surface 15° to the ABS of the airframe centreline as the vortex approaches. (*a*) Rotor phase angle $\psi = 210°$; (*b*) $\psi = 222°$; (*c*) $\psi = 228°$; (*d*) $\psi = 234°$. ○, Kim's (1995) experimental data.

comparisons with Kim's data on top of the airframe in figure 20. As discussed previously, this may result from the relative difficulty in resolving the exact position of the intense vortex, particularly on the RBS side of the airframe. As shown in figure 2(*a*), a small error in predicted position can lead to a large discrepancy in predicted pressure.

5. Discussion and conclusions

Our understanding of the importance of the vortex axial flow and core deformation to accurate prediction of the airframe surface pressure during a collision is substantially improved. Using an axisymmetric helical μ-vortex model, we have shown that axial flow in the vortex core acts to resist vortex thinning and dilation in the region of interaction. This flow also advects the thinned portion of the vortex away from the interaction region while advecting the dilated portion toward the interaction region. The net result is that increased core axial velocity causes reduced vortex thinning, or even thickening, in the region of the vortex–surface interaction, so vorticity is spread over a larger surface area and a more diffuse surface pressure trough is induced. Whether this phenomenon alone can result in the suction reversal observed in experiments as the vortex approaches within a core radius cannot be determined because the results are compromised by modelling that allows vortex vorticity to exist within the solid airframe.

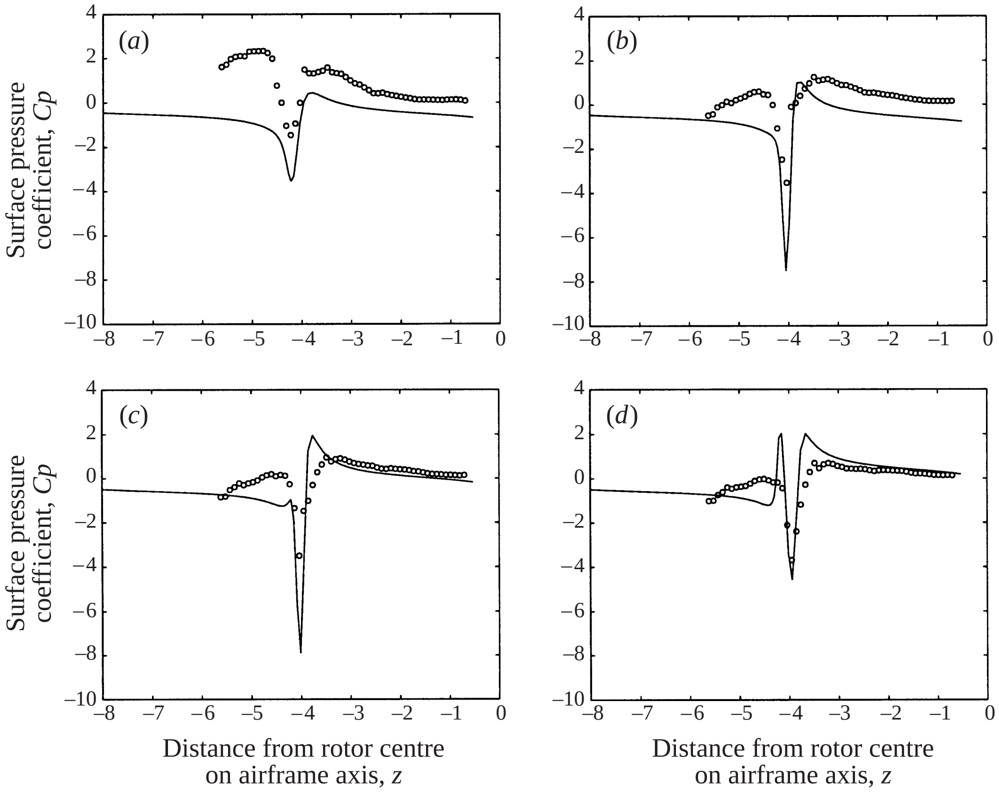

FIGURE 22. Pressure on the airframe surface 15° to the RBS of the airframe centreline as the vortex approaches. (*a*) Rotor phase angle $\psi = 210°$; (*b*) $\psi = 222°$; (*c*) $\psi = 228°$; (*d*) $\psi = 234°$. ○, Kim's (1995) experimental data.

To bound vorticity in the core, the box-vortex model was formulated. In this model, the effects of axial velocity are intrinsically connected to the effects of vortex core flattening. With this model, we see that core flattening without axial velocity distributes vorticity over a larger region of the airframe surface by spreading the vortex core along the airframe axis. This effect gives a broader surface pressure trough of lower magnitude. Adding axial velocity to this model results in less vortex thinning near the surface, as discussed previously. Less vortex thinning means that the vortex must flatten even more to maintain the core cross-sectional area and the vortex centreline-to-airframe separation, so vorticity is distributed more widely still and the surface pressure trough becomes yet more diffuse. Note that flattening of a vortex segment actually increases the core axial velocity even though the core cross-sectional (ξ-η) area remains constant. This occurs because the vortex vorticity component tangential to the airframe surface increases as the core area in the (η, ζ)-plane decreases.

The same trends are predicted when the box-vortex model is applied to the experimental case, although the curvature of the vortex complicates matters somewhat. In previous predictions of the experimental results (Affes *et al.* 1993) the vortex core is seen to thin strongly in the absence of axial core flow, which would delay the onset of vortex flattening. With the current model, the axial velocity first inhibits vortex thinning which subsequently results in prompt initiation of vortex-core flattening. The combination of these two effects allows good prediction of the vortex core height and the width of the surface pressure trough at $x = 0$. As discussed before, the overall surface-pressure predictions appear quite reasonable when one notes that the blade passage effect is not modelled and that very small differences in predicted vortex position on the sides of the airframe, perhaps resulting from inaccuracies in the downwash velocity distribution, can cause large discrepancies in the magnitude of the predicted pressure.

Several changes could improve the numerical predictions. Refinement of experimental measurements applied as boundary or initial conditions for the model would be useful. Particularly, the downwash velocity should be better represented to replace the empirical model used. Spatially varying circulation and axial velocity initial conditions, if known, could also be applied in the current model with little revision.

The principal remaining limitation on the current model is the inability of the panel representation of the airframe to enforce the zero-normal-velocity boundary condition uniformly along the airframe surface as the strong vortex approaches. Vortex segment endpoints are eventually predicted to pass through the airframe boundary, thereby invalidating the velocity prediction and thus any further time advance. Better panel methods, such as interpolation methods discussed by Terzi & Chiu (1997) or adaptive panel griding, would allow computation of the collision to extend further in time. Also, we believe the failure of the present panel model is the principal cause of any remaining pressure integration error. Finally, improvement of the airframe panel boundary condition would allow us to replace the vortex core deformation model, in which the vortex boundary is empirically maintained outside of the airframe, with a model in which the vortex core boundaries are advected by the calculated local velocity.

Further advance of the vortex using our inviscid model will ultimately require modelling of viscous effects. As the vortex segments flatten against the airframe, they will begin to merge with, and become indistinguishable from, the viscous boundary layer on the airframe. The ends of the remaining inviscid vortex segments are then expected to establish a normal terminus on the airframe surface, such as predicted by Lee *et al.* (1998), and propagate along the sides of the airframe under the influence of the rotor downwash, as seen in experiments. The boundary layer will act as a sink for the vortex axial flow on the advancing blade side of the airframe and as a source for the axial flow on the retreating blade side. Eventual reconnection of the vortex ends below the airframe is yet another interesting problem.

The authors wish to recognize and thank the US Army Research Office and Dr Thomas Doligalski for their support through grant DAAH04-93-G0048.

REFERENCES

ABRAMOWITZ, M. & STEGUN, I. A. 1964 *Handbook of Mathematical Functions.* Dover.

AFFES, H. & CONLISK, A. T. 1993 A model for rotor tip vortex–airframe interaction, Part 1: Theory. *AIAA J.* **31**, 2263–2273.

AFFES, H., CONLISK, A. T., KIM, J. M. & KOMERATH, N. M. 1993 A model for rotor tip vortex-airframe interaction, Part 2: Comparison with experiment. *AIAA J.* **31**, 2274–2282.

BATCHELOR, G. K. 1967 *Introduction to Fluid Dynamics.* **81**. Cambridge University Press.

BRAND, A. G. 1989 An experimental investigation of the interaction between a model rotor and airframe in forward flight. PhD thesis, Georgia Institute of Technology.

EGOLF, T. A. & LANDGREBE, A. J. 1983 Helicopter rotor wake geometry and its influence in forward flight. Vol. 1. *NASA CR-3726.*

HESS J. L. & SMITH, A. M. O. 1967 Calculation of potential flow about arbitrary bodies. *Progr. Aero. Sci.* **8**, 1–138.

Hon, T. L. & Walker, J. D. A. 1991 Evolution of hairpin vortices in a shear flow. *Comput. Fluids* **20**, 343–358.

Kim, J. M. & Komerath, N. M. 1995 Summary of the interaction of a rotor wake with a circular cylinder. *AIAA J.* **33**, 470–478.

Lee, J., Burggraf, O. R. & Conlisk, A. T. 1998 On the impulsive blocking of a vortex-jet. *J. Fluid Mech.* **369**, 301–331.

Liou, S. G., Komerath, N. M. & McMahon, H. M. 1990 Measurement of the interaction between a rotor tip vortex and a cylinder. *AIAA J.* **28**, 975–981.

Lorber, P. F. & Egolf, T. A. 1990 An unsteady helicopter rotor-fuselage aerodynamic interaction analysis. *J. Am. Helicopter Soc.* **36**, 32–42.

McAlister, K. W., Schuler, C. A. Branum, L. & Wu, J. C. 1995 3-D wake measurements near a hovering rotor for determining profile and induced drag. *NASA TP-3577.*

Mahalingam, R., Komerath, N. M., Radcliff, T. D., Burggraf, O. R. & Conlisk, A. T. 1997 Vortex-surface collisions: 3-D core flow effects. *AIAA Paper* 97-1785.

Mahalingam, R., Peterson, K., Frank, R. B., Komerath, N. K. & Conlisk, A. T. 1995 Recent experiments on vortex collision with a cylinder. *AIAA Paper* 95-2236.

Moore, D. W. & Saffman, P. G. 1972 The motion of a vortex filament with axial flow. *Phil. Trans. R. Soc.* **272**, 403–429.

Radcliff, T. D., Burggraf, O. R. & Conlisk, A. T. 1997 Axial core flow effects on the interaction of a rotor-tip vortex with an airframe. *AIAA Paper* 97-0658.

Radcliff, T. D., Burggraf, O. R. & Conlisk, A. T. 1999 Use of a deformable core vortex model in predicting vortex-surface interactions. *AIAA Paper* 99-0169.

Scully, M. B. 1975 Computation of a helicopter rotor wake geometry and its influence on rotor harmonic airloads. *Mass. Inst. Tech. ASRL-TR-176-1.*

Terzi A., & Chiu T. W. 1997 Modern panel method techniques for modeling wake-body interference. *AIAA Paper* 97-1829.

Widnall, S., Bliss, D. & Zalay, A. 1971 Theoretical and experimental study of the stability of a vortex pair. In *Aircraft Wake Turbulence and its Detection.* Plenum.

Xiao, Z., Affes, H. & Conlisk, A. T. 1994 The boundary layer flow due to a vortex approaching a cylinder. *J. Fluid Mech.* **275**, 33–58.